

IMPROVED MAGNETIC RESONANCE IMAGING VIA SPARSE  
RECONSTRUCTION AND PHYSICS BASED MODELING

A Dissertation

Presented to the Faculty of the Graduate School  
of Cornell University

In Partial Fulfillment of the Requirements for the Degree of  
Doctor of Philosophy

by

Mitchell Anthony Cooper

JANUARY 2015

© 2015 Mitchell Anthony Cooper

IMPROVED MAGNETIC RESONANCE IMAGING VIA SPARSE  
RECONSTRUCTION AND PHYSICS BASED MODELING

Mitchell Anthony Cooper, Ph. D.

Cornell University 2015

Magnetic Resonance Imaging (MRI) is unique in its ability to image human tissue with varying contrasts and to probe the physical properties of the tissue. In addition, MRI signal is often redundant (or sparse) in nature, especially over time with short update intervals. The goal of this thesis was to better understand and utilize T1relaxation time mapping schemes in the heart to ultimately image infiltrative disease. A second aim was to improve upon state of the art methods for high frame rate liver imaging by utilizing local (patch) based constraints.

## **BIOGRAPHICAL SKETCH**

Mitchell Cooper was born in Mayfield Ohio on February 11<sup>th</sup>, 1987. He followed in the footsteps of his paternal grandfather (Lawrence Cooper; Bachelor of Science in Mechanical Engineering; Case Institute of Technology; 1951) in obtaining his engineering degree from Case Western Reserve University. Merging engineering and medicine, he went on to obtain his PhD from Cornell University, following the path set by his maternal great-grandfather (Anthony Skur; Doctor of Medicine; Cornell College of Medicine; 1927).

Dr. Cooper attended Case Western Reserve University for his Undergraduate Degree from 2005-2009. He majored in Biomedical Engineering with a focus on Medical Imaging. While at Case, Dr. Cooper researched under Dr. Margot Damaser at the Cleveland Clinic Foundation. Dr. Damaser fostered his interest in medical research and encouraged him to attend graduate school.

In the fall of 2009, Dr. Cooper joined the lab of Dr. Yi Wang in the Biomedical Engineering Department at Cornell University. After a year completing courses in Ithaca, he moved to Weill Cornell Medical College in Manhattan to research full time with Dr. Wang. In 2010, he was awarded a prestigious National Science Foundation Fellowship. In 2013, Dr. Cooper began a research project in collaboration with the Cornell Tech. Campus and Dr. Miki Elad at Technion University in Israel.

## DEDICATION

There are many people who have encouraged and guided me through this process and I dedicate this thesis to them.

First, I greatly thank my father Michael and mother Tracey for their love, support, acceptance and guidance in my life. I also would like to thank their spouses Sharon and Charles who entered my life and gave me amazing new perspectives.

I have been supported by great family members throughout my journey and while the list is too long to write here, there are a few that I would like to note. I would like to thank my Uncle Greg and Aunt Barbara whose guidance and encouragement throughout my higher education journey was unparalleled. I would also like to thank my Granny (Theresa Roberts) for her support from the time I was an infant and for ensuring that I received a comprehensive early childhood education. Also for telling stories of her great-grandfather, husband and son who have helped to shape my life. I also want to thank my Aunt Therese for her love and support as my godmother.

Finally, I want to thank my Aunt Jill for inspiring me to achieve greatness and challenging me as a kid writing to me and including math problems and helping me with school projects.

I also have to thank Jonathon and Van Fagert for their unconditional love and support from the day we all met on the first day of undergrad throughout the PhD process.

They have helped to shape me into the person I am today and I am grateful for their continued open door, listening ears, and shoulders to lean on.

I would also like to thank Deborah and Andrew Wallentine, along with Becky and Greg Bullen, who in the past two years have taken me in as a second family and helped me to enjoy life and live it to its fullest even when I was down during my PhD process.

I wouldn't be where I am today if it were not for the great students and faculty in the lab of Dr. Yi Wang. Drs. Thanh Nguyen and Pascal Spincemaille have given endless instruction, guidance and support from the start of the PhD process. They were my guides in the last five years and I would not be here without them. In addition, I would like to thank Drs. Martin Prince and Jonathan Weinsaft for their clinical teachings and many collaborative efforts. I would also like to thank the many students and collaborators I have worked with: Cynthia Wisnieff, Keigo Kawaji, Bo Xu, Alexey Dimov, Jingwei Zheng, Kofi Deh, Sarah Eskris-Winkler, Carlo Salustri, Tian Liu, Noel Codella, Richard Wong, Yanchen Zhu, Jing Liu, Dong Zhou, Nanda Thimmappa, Silvina Dutruel, Mukta Agrawal, Amy Kuceyeski, Esben Plenge, Mengchao Pei, Srikanath Boddu, and Shalini Chhabra. I would like to thank Dr. Miki Elad for his guidance and for sharing his knowledge while working with me to develop PROUD. I would also like to thank Drs. Peter Doerschuk and David Christini for serving on my thesis committee.

Finally, I would like to thank Dr. Yi Wang for bringing me to Cornell and inspiring and guiding me throughout my PhD career. I will never forget and will always use his key teaching “nothing should be treated as a black box”.

Most importantly, I dedicate this to Andrew, my life, my love. You brought me to the finish line. Every day I am with you is a day in paradise.

## ACKNOWLEDGEMENTS

I would like to thank the following for their support throughout my graduate career:

The Cornell Department of Biomedical Engineering

The National Science Foundation Graduate Research Fellowship (DGE-0707428)

The National Institutes of Health HL064647

Joan & Irwin Jacobs Technion-Cornell Innovation Institute

In addition, the works in chapters 3 and 7 has been published or submitted to be published in Magnetic Resonance in Medicine, published by Wiley Periodicals. I have been granted permission to reproduce these works for which the following copyright notice applies:

*© 2013-2014 Wiley Periodicals, Inc. All rights reserved. No part of this publication may be reproduced, stored or transmitted in any form or by any means without the prior permission in writing from the copyright holder. Authorization to copy items for internal and personal use is granted by the copyright holder for libraries and other users registered with their local Reproduction Rights Organization (RRO), e.g. Copyright Clearance Center (CCC), 222 Rosewood Drive, Danvers, MA 01923, USA ([www.copyright.com](http://www.copyright.com)), provided the appropriate fee is paid directly to the RRO. This consent does not extend to other kinds of copying such as copying for general distribution, for advertising or promotional purposes, for creating new collective works or for resale*

## TABLE OF CONTENTS

BIOGRAPHICAL SKETCH .....	iv
DEDICATION .....	v
ACKNOWLEDGEMENTS .....	viii
1 Introduction .....	1
1.1 Summary of Contributions to the Field.....	2
2 MRI Principles .....	3
2.1 MRI Signal Generation .....	3
2.2 Tissue Relaxation Times .....	3
2.3 Pulse Sequence.....	4
2.4 Phased Array Coils.....	5
2.5 Parallel Imaging and Undersampled Image Reconstruction .....	5
2.8 References .....	8
3 FLIP ANGLE PROFILE CORRECTION IN LOOK-LOCKER $T_1$ MAPPING .....	9
3.1 Abstract .....	9
3.2 Introduction .....	9
3.3 Methods.....	11
3.3.1 Effective FA Profile .....	11
3.3.2 Look-Locker IR-SSFP $T_1$ and $T_2$ mapping with FA profile correction.....	12
3.4 Imaging Experiments .....	14
3.5 Data Analysis .....	15
3.6 Results .....	17
3.7 Discussion .....	21
3.8 References .....	27
4 ERROR ANALYSIS IN MOLLI CARDIAC $T_1$ MAPPING .....	33
4.1 Abstract .....	33
4.2 Introduction .....	34
4.3 Material and Methods .....	35
4.3.1 $T_1$ Fitting Approaches for MOLLI Data.....	35
4.3.2 Imaging Experiments .....	37
4.3.3 Data Analysis .....	39
4.4 Results .....	40
4.5 Discussion .....	47
4.6 References .....	52
5 $T_1$ MAPPING OF CARDIAC AMYLOID .....	59
5.1 Introduction .....	59
5.2 Methods .....	59
5.3 Results .....	61
5.4 Discussion .....	64

5.5 References .....	65
6 ACCELERATED CARDIAC IMAGING .....	67
6.1 Introduction .....	67
6.2 Theory .....	67
6.3 Methods .....	69
6.4 Results .....	69
6.5 Discussion .....	72
6.6 References .....	73
7 HIGH SNR HIGH TEMPORAL FRAME RATE LIVER IMAGING.....	75
7.1 Abstract .....	75
7.2 Introduction .....	76
7.3 Theory .....	77
7.4 Methods.....	82
7.4.1 Optimization of reconstruction parameters .....	82
7.4.2 Numerical phantom SNR .....	83
7.4.3 Numerical phantom temporal footprint.....	84
7.4.4 In vivo liver MRI experiments .....	85
7.5 Results .....	86
7.5.1 Parameter selection .....	86
7.5.2 Phantom SNR test .....	87
7.5.3 Phantom temporal footprint .....	87
7.5.4 In vivo testing.....	90
7.6 Discussion .....	92
7.7 Conclusion.....	94
7.8 Appendix A .....	95
7.9 Appendix B .....	96
7.10 References .....	99
8 Future Directions & Conclusion .....	105
8.1 Future Directions.....	105
8.1.1 Cardiac T1 Mapping .....	105
8.1.2 High SNR High Frame Rate Liver Imaging .....	106
8.2 Conclusion.....	107

## CHAPTER 1

### **1 Introduction**

Magnetic Resonance Imaging (MRI) has been advancing clinical diagnostics since Paul Lauterbur first produced an MRI image in the early 1970's. From its advent MRI has been favored as a modality that can not only provide images of the body but also specific information about tissue characteristics. Even before MRI was introduced to provide spatially localized images, NMR was used to characterize materials and tissues. One technique was Look-Locker imaging developed in 1970 by David Look and Donald Locker. This technique utilized a train of RF pulses to measure a specimen's T1 relaxation time in a fast manner. A similar technique was then proposed for MRI in 1992, by Deichmann and Haase to measure in vivo T1 time in static tissue. Since then, multiple techniques have been introduced to characterize T1 and T2 using various pulse sequences and focused on a multitude of anatomies. In 2004, Modified Look Locker Imaging (MOLLI) was introduced by Messroghli to allow for cardiac T1 mapping within one breath hold. This quantitative method has been clinically relevant as of late because standard cardiac MRI methods such as delayed enhancement are not effective at characterizing diffuse disease in which there is no local normal control for visual comparison.

Another overarching theme of MRI has been accelerated MRI imaging. This is evident from the early days of MRI when echo planar imaging was first implemented to allow for fast scans. As the field developed, and hardware as well as computing capabilities improved, parallel imaging using information from multiple RF receiver coils has

allowed for under sampled image reconstruction to reduce scanning time. Early algorithms such as Generalized Series, Keyhole, SMASH and later SENSE and GRAPPA helped to guide the field and are key to fast clinical scans used today. With the advent of compressed sensing a new wave of under-sampled MRI reconstruction has begun opening the door for increasingly fast MRI scans allowing for previously overlooked dynamics to now be imaged and analyzed.

### 1.1 Summary of Contributions to the Field

This work is aimed to provide fast and quantitative cardiac MRI imaging that can be used to characterize diffuse cardiac disease such as amyloid deposition. A second aim is to improve upon current high temporal resolution MRI techniques by incorporating local imaging constraints based on dictionary learning to allow for high SNR high temporal resolution liver MRI imaging. The contributions will be discussed in depth in this thesis:

- 1) Flip angle profile correction in Look-Locker based Steady State Free Precession T1 mapping.
- 2) Error Analysis in Modified Look Locker T1 mapping.
- 3) T1 Mapping of cardiac amyloid deposition
- 4) Accelerated cardiac imaging
- 5) High SNR high temporal frame rate liver imaging

## CHAPTER 2

### 2 MRI Principles

#### 2.1 MRI Signal Generation

Signal ( $S$ ) in magnetic resonance imaging is formed when hydrogen protons within the body are placed in a static magnetic field ( $B_0$ ). The MRI signal equation is shown below (1):

$$S(k_x, k_y) = \iint \rho(x, y) e^{-i2\pi(k_x x + k_y y)} dx dy \quad [2.1]$$

This is the Fourier Transform of the proton density ( $\rho$ ) in the imaging sample.

To localize the MRI signal, linear magnetic field or phase encoding gradients ( $G$ ) are played out. The locations in k-space are denoted in Eq. [2.1] as  $k_x$  or  $k_y$  for the two-dimensional case (1) and can be expanded as:

$$k_{x,y} = \gamma \int_0^t G_{x,y}(t) dt \quad [2.2]$$

Therefore, the path that the signal traverses in k-space is dependent on the gradient in the x and y directions and the amount of time it is played out. Where  $\gamma$  is the gyromagnetic ratio. The gradient waveforms can be played out separate or in unison to create an endless amount of k-space trajectories. Typical trajectories include:

Cartesian, radial and spiral.

#### 2.2 Tissue Relaxation Times

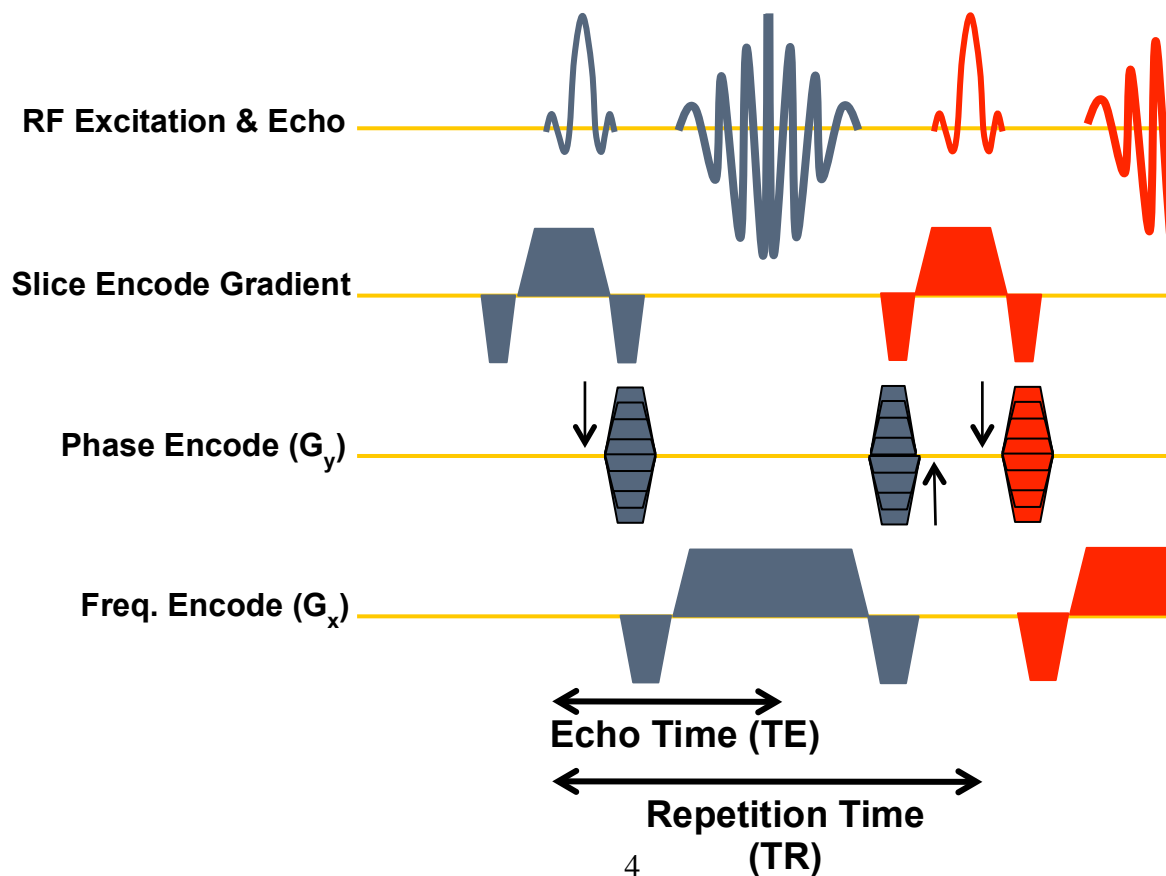
Since each tissue has a varying proton density, each has a unique proton weighting in the MRI image. In MRI, each set of protons is excited by an RF pulse from the  $B_0$  direction into the transverse plane. This deviation excitation is used to produce the

MRI signal. In addition, as the spins are excited, they begin to move back to their equilibrium state. This phenomena is known as relaxation. Due to their composition each tissue will have unique relaxation times that will allow for further probing of tissue contrast. There are two relaxation times that are discussed in this thesis. They are T1, which is the relaxation time relating to the spins returning entirely to the longitudinal plane and T2, which is related to the spin-spin interactions of the protons in the transverse plane (1).

### 2.3 Pulse Sequence

After excitation and gradient encodings, the signal can be read out. These steps can be put together in a pulse sequence. An example of the SSFP pulse sequence is shown below in Figure 2.1.

*Figure 2.1: A Steady State Free Precession (SSFP) pulse sequence diagram..*



## 2.4 Phased Array Coils

Originally, MRI signals were acquired with one RF receiver coil. As coil technology and data storage/processing capabilities have improved, it is now standard to have multiple RF receiver coils. Multiple coils provide many benefits. One obvious benefit is increased SNR due to the multiple samples of the signal from the same physical location. The multiple receiver coils modify Eq. 2.1 by multiplying the proton density ( $\rho$ ) by the coil sensitivity of each RF receiver. The multiple coil images are then combined using the sum of squares of the individual coil images.

## 2.5 Parallel Imaging and Undersampled Image Reconstruction

Another benefit of multiple coil images is the redundant information sampled. With each coil sampling a portion of the same anatomy, only the coil sensitivity profiles in the image are different. Therefore there is a lot of redundant information obtained. This opens the door for under-sampled k-space imaging for reducing scan time. Under the Nyquist sampling theorem, sampling k-space at half the normal rate would induce aliasing in your reconstructed image (see Figure 2.2).

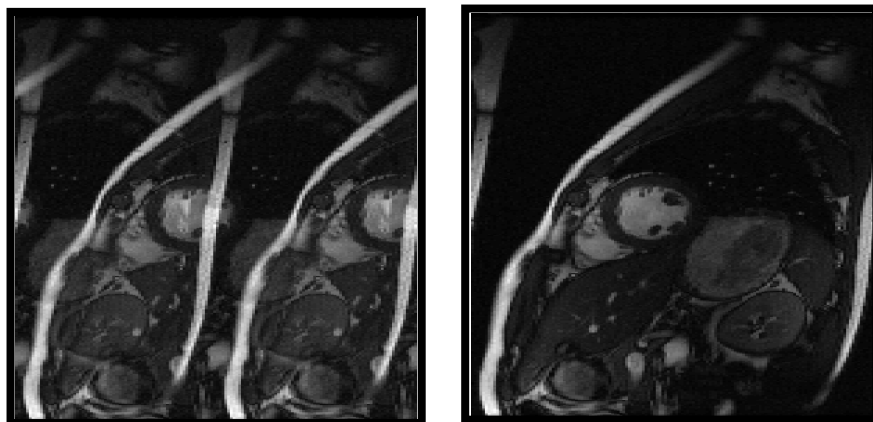


*Figure 2.2: (Left) An image in which every other line was sampled in k-space, resulting in aliasing by half of the field of view in image space. (Right) A fully sampled image.*

However, due to the redundancy in coil data, it is possible to use information about the coils and training data to undo this aliasing and obtain an image similar to the true data in half the time. This concept is called parallel imaging reconstruction.

Various parallel imaging schemes have been developed and some are implemented on clinical scanners. While a survey is beyond the scope of this thesis, the author recommends the following paper for more information:

- *Deshmane A, Gulani V, Griswold MA, Seiberlich N. Parallel MR imaging. J Magn Reson Imaging 2012;36(1):55-72.*

In addition to parallel imaging strategies, constrained optimization problems such as compressed sensing and dictionary learning have proven to be successful at accurately reconstructing under-sampled data as well. While there are hundreds of implementations of these types of methods, a few landmark papers are below:

- *Lustig M, Pauly J. SPIRiT: Iterative Self-consistent Parallel Imaging Reconstruction From Arbitrary k-Space. Magnetic Resonance in Medicine 2010;64(2):457-471.*
- *Ravishankar S, Bresler Y. MR image reconstruction from highly undersampled k-space data by dictionary learning. IEEE Trans Med Imaging 2011;30(5):1028-1041.*

- *Lustig M, Donoho D, Pauly JM. Sparse MRI: The application of compressed sensing for rapid MR imaging. Magn Reson Med 2007;58(6):1182-1195.*
- *Uecker M, Zhang S, Frahm J. Nonlinear inverse reconstruction for real-time MRI of the human heart using undersampled radial FLASH. Magn Reson Med 2010;63(6):1456-1462.*

## 2.8 References

1. Wang, Y. Principles of Magnetic Resonance Imaging. Create Space Online Publishing. 2013. New York, New York. ISBN-10: 1479350419.

## CHAPTER 3

### 3 FLIP ANGLE PROFILE CORRECTION IN LOOK-LOCKER $T_1$ MAPPING<sup>1</sup>

#### 3.1 Abstract

Fast methods using balanced steady-state free precession (SSFP) have been developed to reduce the scan time of  $T_1$  and  $T_2$  mapping. However, flip angle (FA) profiles created by the short RF pulses used in SSFP deviate substantially from the ideal rectangular profile, causing  $T_1$  and  $T_2$  mapping errors. The purpose of this study was to develop a FA profile correction for  $T_1$  and  $T_2$  mapping with Look-Locker 2D inversion recovery SSFP and to validate this method using 2D spin echo as a reference standard. Phantom studies showed consistent improvement in  $T_1$  and  $T_2$  accuracy using profile correction at multiple FAs. Over six human calves, profile correction provided muscle  $T_1$  estimates with mean error ranging from excellent (-0.6%) at  $TR/FA = 18 \text{ ms}/60^\circ$  to acceptable (6.8%) at  $TR/FA = 4.9 \text{ ms}/30^\circ$ , while muscle  $T_2$  estimates were less accurate with mean errors of 31.2% and 47.9%, respectively.

#### 3.2 Introduction

Inversion recovery spin echo (IR-SE) is an accurate method for  $T_1$  mapping but is limited in clinical application due to its prohibitively long acquisition time. To overcome this limitation, a number of fast  $T_1$  mapping methods using gradient echo (GRE) sequences have been proposed. These methods follow the transient

---

<sup>1</sup> Published as: Cooper MA, Nguyen TD, Spincemaille P, Prince MR, Weinsaft JW, et al. (2012) Flip angle profile correction for  $T_1$  and  $T_2$  quantification with look-locker inversion recovery 2D steady-state free precession imaging. *Magn Reson Med* 68:

magnetization after an inversion or saturation pulse, such as the Look-Locker method (LL) (1-4), or utilize the steady-state magnetization, such as the driven equilibrium single pulse observation of T1 (DESPOT1) method (5), or they are a combination of both (6,7). 2D inversion recovery balanced SSFP (IR-SSFP) is a promising approach due to the higher SNR efficiency of SSFP when compared to spoiled GRE (8) and can provide T2 estimations in addition to T1 (7). IR-SSFP has been used to perform fast T1 mapping in skeletal muscle (9).

There are a number of inherent challenges in these fast T1 mapping methods. Short radiofrequency (RF) excitation pulses are often used to reduce the repetition time (TR), especially for time-sensitive applications such as breath-hold myocardial T1 mapping (4,10-12). It is well known that the flip angle (FA) profile of a short slice-selective RF pulse can deviate substantially from the ideal rectangular profile. Because MR signal depends on the FA, the non-ideal FA profile introduces a bias in the estimated relaxation times when not properly accounted for in the signal fitting. This problem has been addressed for T1 mapping using dual FA 2D spoiled GRE imaging (13). In addition, FA profile correction has been investigated for T1 mapping using 3D spoiled GRE LL imaging (14,15). However, this method is specific to 3D imaging and assumes that the signal of a voxel is generated by a single FA determined by the position of that voxel along the slice direction. FA profile correction has not been investigated for 2D IR-SSFP, where a range of different FAs contribute to the signal of each voxel. Therefore, the purpose of this study was to develop and validate a

signal fitting algorithm that takes into account the non-ideal FA profile for 2D LL IR-SSFP T1 and T2 mapping.

### 3.3 Methods

#### *3.3.1 Effective FA Profile*

Given a shaped RF pulse with magnitude  $B_1(t)$  and phase  $\varphi(t)$  in the rotating frame and a constant slice-select gradient  $G_z(t) = G$ , the resultant magnetization along the slice direction  $\mathbf{M}(z)$  can be calculated by using the hard pulse approximation (16,17) as follows:

$$\mathbf{M}(z) \cong \left( \prod_{i=0}^{N-1} \mathbf{R}_z(\psi) \mathbf{R}_z(\varphi_i) \mathbf{R}_x(\vartheta_i) \mathbf{R}_z(-\varphi_i) \right) \mathbf{M}_0(z) \quad [3.1]$$

$$\psi = \gamma G z \Delta t \quad \varphi_i = \varphi(i\Delta t) \quad \vartheta_i = \gamma B_1(i\Delta t) \Delta t$$

where  $\mathbf{M}(z) = [M_x \ M_y \ M_z]^T$  represents the magnetization vector,  $N$  is the number of discretizing hard pulses,  $\Delta t$  is the interval between hard pulses,  $\mathbf{R}_x$  and  $\mathbf{R}_z$  denote the rotation matrices around  $x$  and  $z$  axis, respectively, and  $\mathbf{M}_0(z) = [0 \ 0 \ 1]^T$  is the initial equilibrium magnetization. Note that off-resonance and relaxation effects are ignored in Eq.3.1 (this simplification is justified when the RF pulse width is short as in this study). The transverse magnetization  $M_{xy}(z)$  at the end of the excitation and the corresponding effective FA profile  $\alpha(z)$  are then given by:

$$M_{xy}(z) = (M_x^2 + M_y^2)^{1/2}$$

$$\alpha(z) = \arcsin(M_{xy}(z)) \quad [3.2]$$

As an example, Fig.3.1 shows a Hamming filtered half-sinc RF pulse (17) with a 60° nominal FA and its effective FA profile.

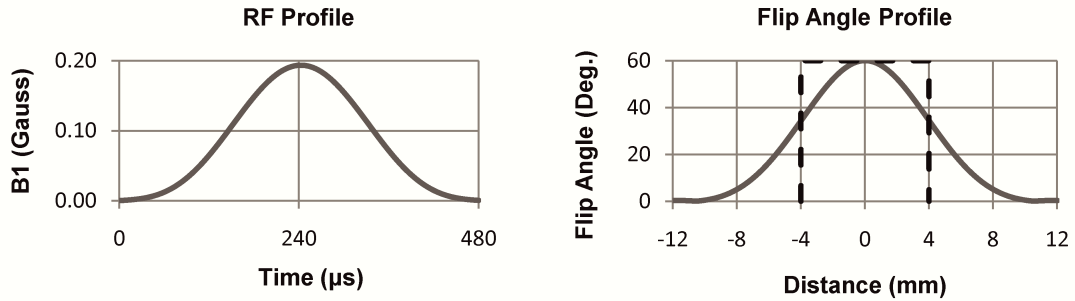


Figure 3.1: RF profile of a half-sinc excitation pulse (apodized with a Hamming window) with a 60° nominal FA (left) and corresponding effective FA profile calculated using Bloch simulation (right). The dashed line shows the ideal rectangular FA profile over the slice thickness used in our imaging experiments (8 mm).

### 3.3.2 Look-Locker IR-SSFP T1 and T2 mapping with FA profile correction

This study implemented a 2D IR-SSFP sequence for LL T1 mapping. One LL period of this sequence consists of a non-selective hard inversion pulse and spoiler gradients, followed by 6 Kaiser-Bessel-ramped RF pulses prior to uninterrupted SSFP readout, and concluded by a sufficiently long time delay to allow the excited magnetization to return to equilibrium before the next period. The Kaiser-Bessel ramp provided a short and effective magnetization preparation for subsequent SSFP readout (18,19). A short hard pulse was used for longitudinal magnetization inversion instead of a long adiabatic pulse as it is difficult to quantify the inversion efficiency of an adiabatic pulse for short T2 tissues such as muscle (20). Given T1, T2, M<sub>0</sub> and pertinent

sequence parameters (including the shapes of the imaging RF pulses), Bloch simulation can be used to follow the evolution of the magnetization over the course of the experiment and to calculate the transverse SSFP signal  $S$  (10,21) as follows (ignoring off-resonance effects):

$$S(n, T_1, T_2, M_0) = \int_z [(S_0(z) - S_{ss}(z))\lambda(z)^n + S_{ss}(z)]dz \quad [3.3]$$

where

$$\lambda(z) = \frac{\cos(\alpha(z))(E_1 - E_2) + \sqrt{\cos^2(\alpha(z))(E_1 - E_2)^2 + 4E_1E_2}}{2}, \quad [3.4]$$

and the steady state transverse magnetization is given by

$$S_{ss}(z) = M_0 \frac{\sqrt{E_2}(1 - E_1)\sin(\alpha(z))}{1 - (E_1 - E_2)\cos(\alpha(z)) - E_1E_2} \quad [3.5]$$

Here  $n$  is the index of the SSFP readouts,  $S_0(z)$  is the transverse signal at time  $TE$  in the first readout that follows the inversion pulse, spoiler gradients and the 6 Kaiser-Bessel ramp-up preparation,  $E_1 = \exp(-TR/T_1)$ ,  $E_2 = \exp(-TR/T_2)$ ,  $M_0$  is a scaling factor (which includes the proton density and receiver sensitivity),  $\alpha(z)$  is the flip angle at position  $z$  along the slice direction, and  $\lambda$  denotes the relaxation rate of the SSFP signal evolution (10,21). Note that Eq. 3.3 is similar to Eq.6 in (21) or approach 2 in (10) (with a more generalized  $S_0(z)$  due to the use of a 6 Kaiser-Bessel ramp in this work), where the length of the SSFP readout is assumed to be long enough to allow the transverse magnetization to reach steady state, and the time delay between the end of the SSFP readout and the start of the next inversion pulse is long enough to allow a full relaxation of the longitudinal magnetization. Both of these conditions were met in

our study. Eq. 3.4 is the same as Eq. 5 in (21) except for the factor of 2 in the denominator, which was missing in (21). For  $TR \ll T_1, T_2$ , the formula for  $\lambda$  can be simplified as in Refs (10) and (21) (this simplification was not used in this study). It is important to note the dependency of  $S_0(z)$ ,  $S_{ss}(z)$  and  $\lambda(z)$  on the position  $z$  along the slice direction. Given the measured noisy SSFP data, denoted by  $S^*(n)$ ,  $T_1$ ,  $T_2$  and  $M_0$  can be obtained by minimizing the sum of squared differences between the measured and expected signals:

$$T_1, T_2, M_0 = \arg \min_n \sum_n (S^*(n) - S(n, T_1, T_2, M_0))^2 \quad [3.6]$$

### 3.4 Imaging Experiments

All experiments were performed at 1.5T (GE HDxt 15.0). For phantom imaging, four water tubes were doped with manganese chloride ( $MnCl_2$ ) at 0.4, 0.2, 0.1, and 0.04 mM concentrations. For the volunteer study, the calf muscles of six healthy volunteers (4 male, 2 female, mean age of 26 years  $\pm$  3 [standard deviation (SD)]) were scanned. The study was approved by the local IRB and informed consent was obtained from all subjects prior to imaging.

IR-SSFP imaging parameters were as follows:  $TR = 5-5.4$  ms (phantoms)/4.9 (humans);  $TE = TR/2$  (symmetric full echo); nominal  $FA = 30^\circ, 60^\circ, 90^\circ$  (phantoms) /  $30^\circ, 60^\circ$  (humans);  $FOV = 25$  cm (phantoms)/26-30 cm (humans), partial phase  $FOV$  factor = 0.5, matrix = 256x128, slice thickness = 8 mm, readout bandwidth =  $\pm 62.5$  kHz. To investigate the magnetization transfer (MT) effect of  $TR$  and  $FA$  on the SSFP signal of skeletal muscle tissue as suggested previously (22), subjects were also

scanned with a long TR of 18 ms and FA of 30° and 60°. In addition, one volunteer was scanned using a FA of 90°. An 8-channel cardiac phased-array receive coil was used for all experiments. A Hamming filtered half-sinc pulse (17), which is the standard RF excitation pulse for the product 2D SSFP sequence on our system, was used in all experiments. Each scan consisted of multiple LL periods, and the length of each period is the time between consecutive inversion pulses and consisted of 1) an SSFP readout following the inversion pulse consisting of either 1024 SSFP TRs when using TR ~5 ms or 512 TRs when using TR = 18 ms to allow the transverse magnetization to reach steady state, and 2) a time delay between the end of the SSFP readout and the next inversion pulse (about 9 sec for phantoms and 5-6 sec for human imaging) to allow a full relaxation of the longitudinal magnetization. For 128 phase encodes and 0.5 partial phase FOV, 16 LL periods were required to complete the scan. The length of one LL period was 14 sec for phantoms and 10/15 sec (TR = 4.9/18 ms) for humans, with corresponding scan times of 3.7 min and 2.7/4 min, respectively. For comparison, standard 2D single-echo IR-SE and SE imaging with matching FOV and spatial resolution were performed to obtain the reference standard T1 and T2 values, respectively. B1 maps were also obtained in humans using the double FA method (23) for nominal FA error correction in LL data fitting.

### 3.5 Data Analysis

A look-up table method was used to correct for signal bias due to Rayleigh noise in sum-of-squares magnitude images obtained with a multiple receiver coil (Fig. 2 in Ref (24)). This correction is particularly important for data points near the zero-crossing

where the signal amplitudes are low. The negative polarity of the data points before zero-crossing was then restored by using the method proposed in (25). B1 correction was performed before fitting for T1 to account for imperfections in the inversion and imaging flip angle. In human subjects, an ROI was selected in the soleus muscle with uniform signal intensity and free of image artifacts. Signals were averaged over a 3x3 neighborhood before fitting to reduce noise effects. Bloch simulation was used to calculate the flip angle profile obtained directly from the scanner, which was a Hamming windowed half-sinc pulse. LL data fitting without FA profile correction was also implemented by assuming a rectangular FA profile in Eqs. 3.3-3.5. In addition, voxel-wise T1 and T2 maps were obtained from all subjects. Processing was performed in MATLAB (Mathworks, Natick, MA) using a Dell PowerEdge R910 computer with 32 cores. The Nelder-Mead unconstrained non-linear solver was used for fitting and a non-linear least-squares fitting was used to obtain the reference T1 and T2 values from the spin echo data. Relative fitting residual, defined as  $\frac{\| \text{Signal}_{\text{measured}} - \text{Signal}_{\text{fitted}} \|_2}{\| \text{Signal}_{\text{measured}} \|_2} \times 100$ , was calculated to measure the quality of the fit. Relative T1 and T2 errors were defined as  $\frac{\| T1_{\text{IR-SSFP}} - T1_{\text{IR-SE}} \|_2}{\| T1_{\text{IR-SE}} \|_2} \times 100$  and  $\frac{\| T2_{\text{IR-SSFP}} - T2_{\text{SE}} \|_2}{\| T2_{\text{SE}} \|_2} \times 100$ . A two-tailed paired sample t-test was used to assess the differences in T1 and T2 values obtained with IR-SSFP and reference methods. A P value of less than 0.05 was considered statistically significant.

### 3.6 Results

T1/T2 values of the four MnCl<sub>2</sub> phantoms obtained with reference standard SE methods were 304/30, 589/67, 919/121, 1532/275 ms. Figure 2a shows the relative T1 and T2 errors in the phantoms obtained with 2D LL IR-SSFP with and without FA profile correction, demonstrating consistently improved accuracy with the profile correction method for both T1 and T2, as well as increasingly larger T1 errors at higher FAs when profile correction was not used. Overall T1 errors were less than 5.8% when fitting with profile correction for FA range of 30°-90°, while T1 error could be as high as 22.7% when fitting without profile correction. Fitting with profile correction provided relative T2 error magnitudes in the range of 2.7-32.3%, while fitting without profile correction yielded much larger T2 error ranging from 91.1% to 177.9%. The differences in T1 and T2 errors obtained with and without profile correction were statistically significant for all FAs (P<0.005). Fitting residuals obtained without profile correction for FA of 60° and 90° were significantly higher than those obtained with profile correction, indicating poorer fits between the measured data and the signal model when FA profile is ignored (Fig. 3.2b).

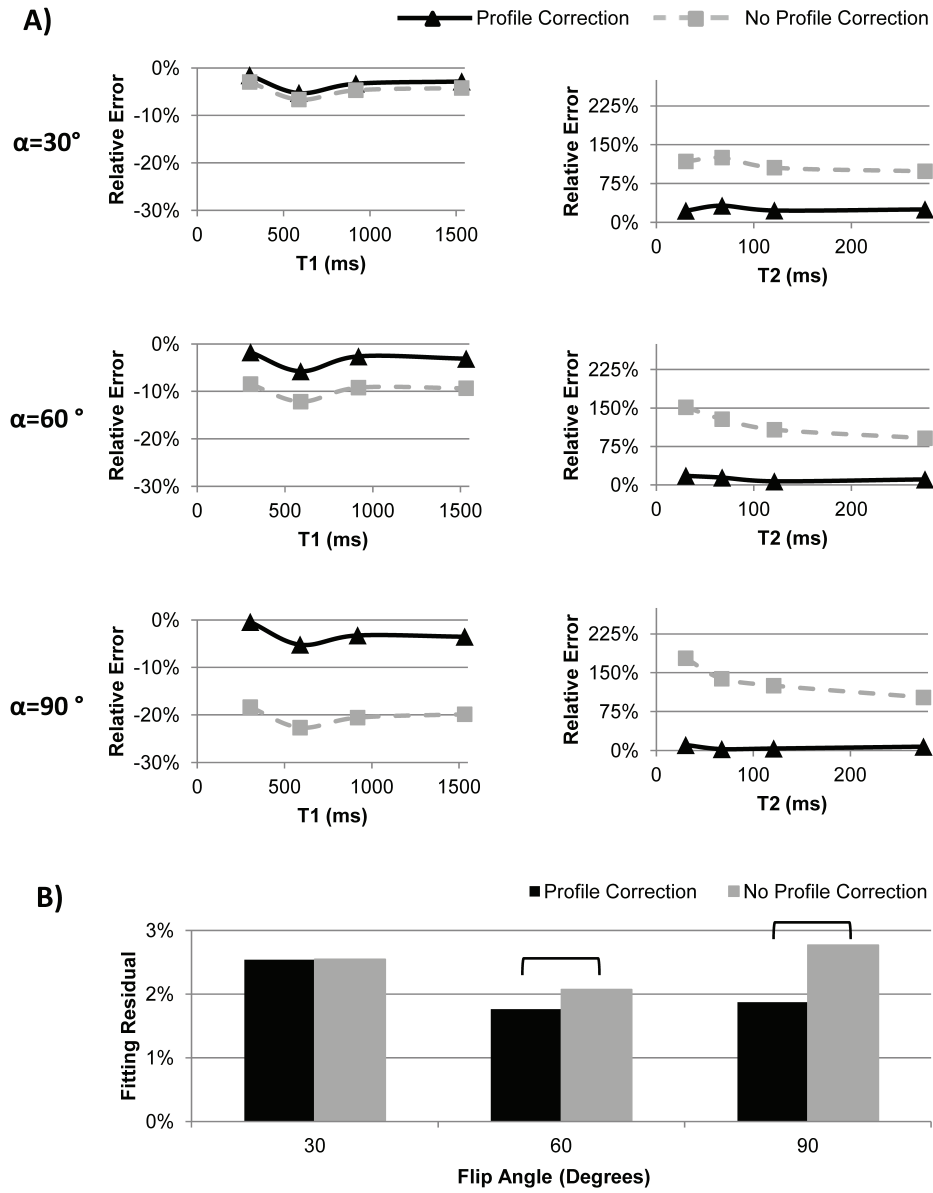


Figure 3.2: A) Relative  $T_1$  and  $T_2$  errors obtained with Look-Locker 2D IR-SSFP with (solid line) and without (dashed line) FA profile correction at  $30^\circ$ ,  $60^\circ$ , and  $90^\circ$  nominal FAs on four  $MnCl_2$  phantoms. Reference  $T_1$  and  $T_2$  values were obtained with reference standard SE methods. B) Comparison of relative fitting residuals averaged over all four phantoms obtained with and without profile correction. Brackets indicate statistical significance ( $p < 0.05$ ). Note the increasingly larger fitting residuals obtained without profile correction as FA becomes larger than  $60^\circ$ , indicating that the assumption of constant FA profile becomes less adequate for this FA regime.

Figure 3.3 shows the effects of FA and TR on T1 error and fitting residual obtained in the calf muscle of one subject with FA profile correction. Note the small error and good fits obtained with a long TR of 18 ms or a small FA of 30°; however, unlike the trend observed in water phantoms (Fig. 3.2), shortening TR to 4.9 ms and employing a FA larger than 60° lead to much larger errors and poorer fits.

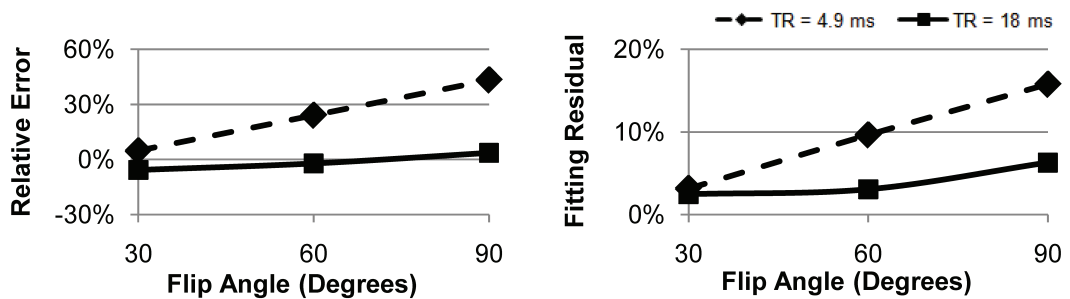


Figure 3.3: Relative  $T_1$  error (left) and fitting residuals (right) obtained with FA profile correction in the calf muscle of one volunteer with a short TR of 4.9 ms (dashed line) and a long TR of 18 ms TR (solid line) at different FAs. Note the increasingly larger errors and worse fits at shorter TR or higher FA, most likely due to larger MT effect in the muscle tissue in this regime (see Discussion section).

Table 3.1 summarizes T1 and T2 values obtained with Look-Locker 2D IR-SSFP and reference standard SE methods in human calves (N=6) using ROI analysis. FA profile correction at 60° with an 18 ms TR provided excellent T1 estimates ( $-0.6 \pm 1.8\%$  error) and T2 estimates with moderate accuracy ( $-31.2 \pm 5.0\%$  or  $-9.5 \pm 1.2$  ms error), representing a 94% and 80% improvement in accuracy for T1 and T2, respectively, when compared with results obtained without profile correction. Profile correction at 30° with a short 4.9 ms TR yielded less accurate results with a relative error of  $6.8 \pm$

2.2% for T1 and  $-47.9 \pm 2.3\%$  for T2. Interestingly, fitting without profile correction at this FA and TR provided more accurate T1 ( $4.8 \pm 2.1\%$  error) and T2 ( $25.8 \pm 4.1\%$  error) estimates. Figure 3.4 shows voxel-wise T1 and T2 maps generated by the proposed fitting method with profile correction. Average fitting time was 23 msec per voxel.

	<b>SE-based</b>	<b>IR-SSFP</b>		<b>IR-SSFP</b>	
	<b>reference</b>	FA=30° TR=4.9 ms		FA=60° TR=18 ms	
	<b>standard</b>	<b>Profile</b>	<b>No Profile</b>	<b>Profile</b>	<b>No Profile</b>
T <sub>1</sub>	985 ± 6	1052 ± 16	1033 ± 15	979 ± 20	874 ± 19
P		<.001	.002	.44	<.001
T <sub>2</sub>	31 ± 2	16 ± 1	39 ± 3	21 ± 2	78 ± 5
P		<.001	<.001	<.001	<.001

*Table 3.1: T1 and T2 (mean ± standard deviation) values of human calf muscle obtained with Look-Locker 2D IR-SSFP based methods with and without FA profile correction using ROI analysis (N=6). Two combinations of short TR/low FA and long TR/high FA were chosen for SSFP to minimize potentially confounding MT effect in muscle. Also shown are values obtained with reference standard SE based T1 and T2 mapping methods.*

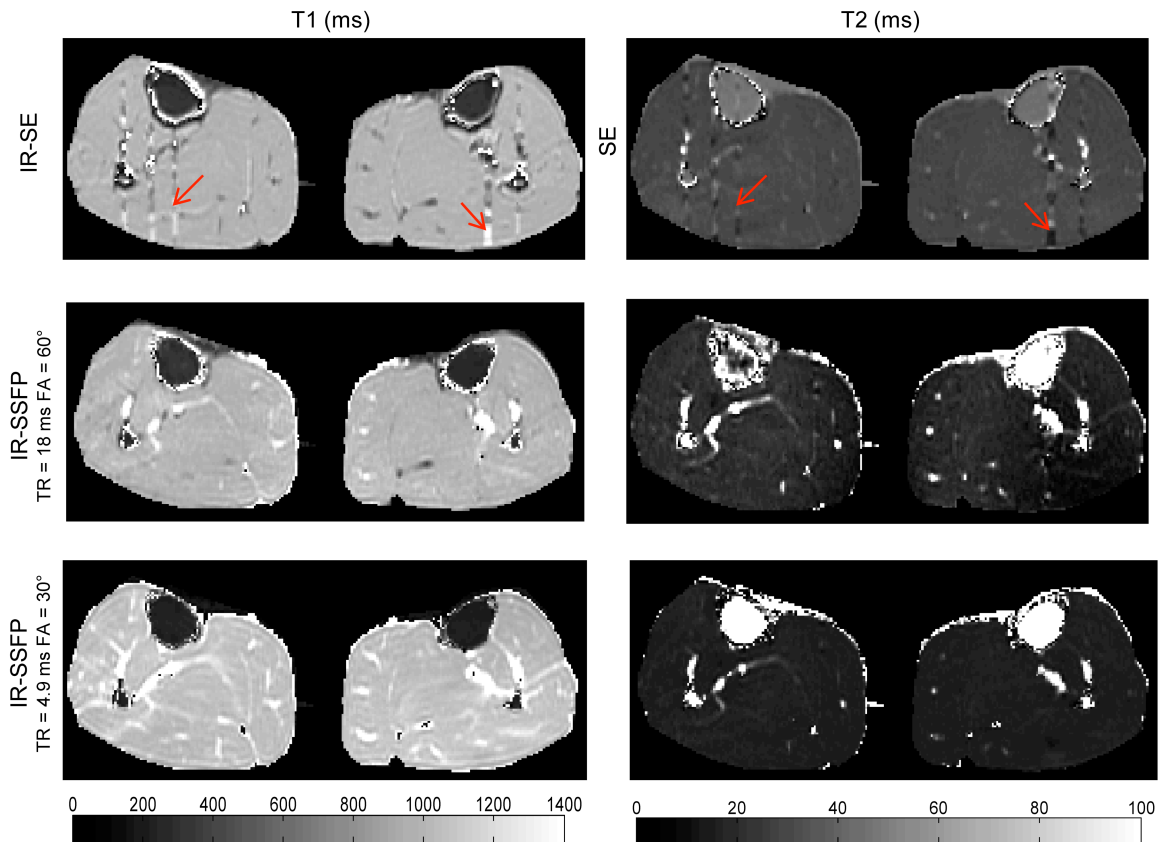


Figure 3.4: Example of T1 and T2 maps obtained with reference standard SE methods (top row) and with Look-Locker IR-SSFP and FA profile correction in the calf of one volunteer using TR/FA=18 ms/60° (middle row) and 4.9 ms/30° (bottom row). T1 maps were very similar between the reference standard and IR-SSFP at 18 ms/60° except in the areas affected by blood flow (red arrows). The T1 map obtained with 4.9 ms/30° appears more noisy. T2 maps are generally less accurate than T1 maps.

### 3.7 Discussion

Our preliminary phantom and human results demonstrate that FA profile correction can greatly reduce errors in T1 and T2 mapping using the Look-Locker 2D IR-SSFP sequence. The improvement in both T1/T2 accuracy and fitting agreement is most

obvious on water phantoms covering a wide range of T1/T2 values. In human calf muscles, the proposed method provided T1 estimates with accuracy ranging from excellent (-0.6% error) to acceptable (6.8% error) depending on the combination of TR and FA, while the T2 estimates were generally less accurate. While the effect of a non-ideal FA profile on T1 mapping has been studied in the context of spoiled GRE imaging (13), the method developed here confirms the importance of FA profile correction for Look-Locker 2D SSFP based T1 mapping with a shaped RF pulse, which is often ignored (4,10).

In this study, we observed increased T1 errors and larger fitting residuals in the calf muscle when a short TR of 4.9 ms was used in combination with a FA higher than 60° (Fig. 3.3). However, this trend was not present in water phantoms (Fig. 3.2). This discrepancy between phantom and in vivo results suggests the presence of on-resonance MT effect in muscles described previously by Bieri and Scheffler (22). Specifically, unlike the free water in phantoms, skeletal muscle tissue can be modeled with a binary spin-bath model with energy exchange between the two spin compartments. This exchange is a function of sequence TR and FA and leads to signal deviating from that derived from the Bloch equation for a single compartment. For our T1/T2 mapping application, employing a lower FA lessens this effect, but also reduces the dynamic range of the transient signal curve, making T1/T2 quantification more sensitive to noise. Using a longer TR also helps mitigate the MT effect, allowing for higher FAs to be used (Fig. 3.3) for improved robustness against noise, but at the cost of increased SSFP off-resonance artifacts. The long TR/high FA and short TR/low FA

acquisitions demonstrated the effects of MT and FA profile. We should note that the IR-SSFP experiment with TR = 18 ms was performed purely to validate our hypothesis regarding the MT effect. Off-resonance effects were minimized by performing a volume shim targeting the small imaging volume and accordingly only minor banding artifacts were observed in one leg which was excluded from ROI analysis. For general T1 mapping, however, the use of a low FA to mitigate the MT effect is recommended.

As MT tends to suppress SSFP signal, the non-ideal FA profile tends to increase the SSFP signal, and these opposite effects may accidentally cancel each other out, resulting in good T1/T2 estimate even if both effects are ignored in the signal model. Our fairly accurate in vivo T1 results obtained without profile correction using a 4.9 ms TR and 30° FA demonstrate this phenomenon. Accordingly, care should be exercised when changing these sequence parameters to avoid errors or when applied to different tissues. We should note that while the MT effect has been shown to have a detrimental effect on spoiled GRE based T1 quantification (26), previous works on IR-SSFP based T1 mapping often utilized a high FA (e.g., 50°) and ignored this effect in their signal models (4,7,10). A method has been proposed (27) for a multi-component relaxometry method which accounts for MT effect in the SSFP signal model. However, this method requires multiple FAs (up to 15), potentially leading to long scanning times. Other authors have used small FAs (10° in (28) and 35° in (29)) for IR-SSFP based T1 mapping, but did not consider the MT effect. Finally, we should note that shortened tissue T1 will reduce the MT effect (22), thereby increasing the need for FA profile correction in post-contrast T1 mapping.

Although both T1 and T2 mapping can be obtained simultaneously with our method, T2 accuracy was found to be limited. For in vivo imaging with a 30° nominal FA, the relaxation is primarily dominated by T1 effect and becomes less dependent on FA profile (see Fig.2 in Ref 17). As T2 mapping is sensitive to off-resonance effects in IR-SSFP (7), the limited T2 accuracy may also be explained by the omission of  $B_0$  correction in the signal fitting algorithm. Despite these challenges, improved T2 accuracy was obtained with FA profile correction in this work.

T1 quantification using Look-Locker 2D IR-SSFP has been investigated previously. Our work follows the approach in (10), in which a Bloch equation based SSFP signal fitting algorithm was implemented for post-contrast myocardial T1 mapping. Here, we introduced FA profile correction and provided an in vivo comparison with reference standard T1 and T2 mapping methods. A three-parameter mono-exponential curve fitting was proposed in (4) to obtain an apparent relaxation rate  $T1^*$  which is then corrected using a formula originally proposed in (3) for IR spoiled GRE (FLASH) acquisition. The applicability of this correction to IR-SSFP has not been elucidated. The average T1 value of skeletal muscle obtained in normal volunteers reported in (4) was 780 ms, which corresponds to a 22% underestimation compared to other relaxometry studies (30,31). A SSFP-based correction formula for T1 was introduced in (7) which was derived from prior work on SSFP transient signal behavior in (21). This method only applies to an IR-SSFP acquisition prepared with a half-alpha RF pulse. In our study, we found that a half-alpha preparation led to severe ghosting

artifacts and accordingly decided to use a 6 Kaiser-Bessel ramp preparation which has been shown to be more robust against off-resonance effects (18,19).

The proposed fitting algorithm requires SSFP signal integration over the FA profile (Eq. 3.3) at each iteration step and accordingly the computational demand is higher than previous methods (13,32). Parker et al proposed a fast look-up table technique for T1 mapping using dual FA 2D spoiled GRE imaging, but this approach becomes non-trivial when multiple parameters ( $T_1$ ,  $T_2$ ,  $M_0$ ) need to be estimated such as in IR-SSFP. We have explored several venues to reduce the fitting time. First, the number of points required for discretizing the FA profile was optimized and as few as 11 points along the profile was found to provide accurate results. Since the FA profile is symmetric for the RF pulse used in this study, signal computation only needs to be carried out for half of the profile. Second, as the fitting of multiple voxels is highly parallelizable, a multi-core version of our algorithm was implemented, achieving an average fitting time of 23 msec per voxel. Further optimization and implementation of the fitting algorithm using a general-purpose programming language such as C may offer further reduction in fitting time.

This study has several limitations. The effects of  $B_0$  inhomogeneity, which may not be ignored at higher field strengths or in other organs such as the heart, were not considered. However,  $B_0$  maps can be acquired and incorporated into the Bloch equation based signal fitting algorithm. Additionally, while  $B_1$  mapping can improve T1 and T2 accuracy against FA error of the inversion and imaging RF pulses (e.g., due

to imperfect prescan), this method requires extra scan time. Also, we only investigated the half-sinc pulse, which is the standard RF excitation pulse for the product 2D SSFP sequence on our scanner. The effect of other RF pulses can be calculated similarly using the hard pulse approximation approach.

In conclusion, FA profile correction significantly improves T1 and T2 quantification with 2D LL IR-SSFP relaxometry and the MT effect in skeletal muscle tissues needs to be considered during pulse sequence design and/or signal fitting for accurate results.

### 3.8 References

1. Look DC, Locker DR. Time Saving in Measurement of NMR and EPR Relaxation Times. *Review of Scientific Instruments* 1970;41(2):250-251.
2. Crawley AP, Henkelman RM. A comparison of one-shot and recovery methods in T1 imaging. *Magn Reson Med* 1988;7(1):23-34.
3. Deichmann R, Haase A. Quantification of T1 values by SNAPSHOT-FLASH NMR imaging. *Journal of Magnetic Resonance (1969)* 1992;96(3):608-612.
4. Messroghli DR, Radjenovic A, Kozerke S, Higgins DM, Sivananthan MU, Ridgway JP. Modified Look-Locker inversion recovery (MOLLI) for high-resolution T1 mapping of the heart. *Magnetic Resonance in Medicine* 2004;52(1):141-146.
5. Deoni SC, Peters TM, Rutt BK. High-resolution T1 and T2 mapping of the brain in a clinically acceptable time with DESPOT1 and DESPOT2. *Magn Reson Med* 2005;53(1):237-241.
6. Tong CY, Prato FS. A novel fast T1-mapping method. *J Magn Reson Imaging* 1994;4(5):701-708.

7. Schmitt P, Griswold MA, Jakob PM, Kotas M, Gulani V, Flentje M, Haase A. Inversion recovery TrueFISP: quantification of T(1), T(2), and spin density. *Magn Reson Med* 2004;51(4):661-667.
8. Scheffler K, Lehnhardt S. Principles and applications of balanced SSFP techniques. *Eur Radiol* 2003;13(11):2409-2418.
9. de Sousa PL, Vignaud A, Fleury S, Carlier PG. Fast Monitoring of T(1), T(2), and Relative Proton Density (M(0)) Changes in Skeletal Muscles Using an IR-TrueFISP Sequence. *Journal of Magnetic Resonance Imaging* 2011;33(4):921-930.
10. Goldfarb JW, Mathew ST, Reichek N. Quantitative breath-hold monitoring of myocardial gadolinium enhancement using inversion recovery TrueFISP. *Magnetic Resonance in Medicine* 2005;53(2):367-371.
11. Higgins DM, Ridgway JP, Radjenovic A, Sivananthan UM, Smith MA. T1 measurement using a short acquisition period for quantitative cardiac applications. *Medical Physics* 2005;32(6):1738-1746.
12. Piechnik SK, Ferreira VM, Dall'Armellina E, Cochlin LE, Greiser A, Neubauer S, Robson MD. Shortened Modified Look-Locker Inversion recovery (ShMOLLI) for clinical myocardial T1-mapping at 1.5 and 3 T within a 9 heartbeat breathhold. *J Cardiovasc Magn Reson* 2010;12:69.

13. Parker GJM, Barker GJ, Tofts PS. Accurate multislice gradient echo T1 measurement in the presence of non-ideal RF pulse shape and RF field nonuniformity. *Magnetic Resonance in Medicine* 2001;45(5):838-845.
14. Siversson C, Tiderius CJ, Dahlberg L, Svensson J. Local flip angle correction for improved volume T1-quantification in three-dimensional dGEMRIC using the Look-Locker technique. *J Magn Reson Imaging* 2009;30(4):834-841.
15. Siversson C, Tiderius CJ, Neuman P, Dahlberg L, Svensson J. Repeatability of T1-quantification in dGEMRIC for three different acquisition techniques: two-dimensional inversion recovery, three-dimensional look locker, and three-dimensional variable flip angle. *J Magn Reson Imaging* 2010;31(5):1203-1209.
16. Pauly J, Le Roux P, Nishimura D, Macovski A. Parameter relations for the Shinnar-Le Roux selective excitation pulse design algorithm [NMR imaging]. *IEEE Trans Med Imaging* 1991;10(1):53-65.
17. Bernstein MA, King KF, Zhou XJ. *Handbook of MRI pulse sequences*. Burlington, MA: Elsevier Academic Press; 2004. xxii, 1017.
18. Le Roux P. Simplified model and stabilization of SSFP sequences. *J Magn Reson* 2003;163(1):23-37.

19. Nguyen TD, Spincemaille P, Prince MR, Wang Y. Cardiac fat navigator-gated steady-state free precession 3D magnetic resonance angiography of coronary arteries. *Magn Reson Med* 2006;56(1):210-215.
20. Norris DG, Ludemann H, Leibfritz D. An Analysis of the Effects of Short T2 Values on the Hyperbolic-Secant Pulse. *Journal of Magnetic Resonance* 1991;92(1):94-101.
21. Scheffler K. On the transient phase of balanced SSFP sequences. *Magnetic Resonance in Medicine* 2003;49(4):781-783.
22. Bieri O, Scheffler K. On the origin of apparent low tissue signals in balanced SSFP. *Magn Reson Med* 2006;56(5):1067-1074.
23. Stollberger R, Wach P. Imaging of the active B1 field in vivo. *Magn Reson Med* 1996;35(2):246-251.
24. Constantinides CD, Atalar E, McVeigh ER. Signal-to-noise measurements in magnitude images from NMR phased arrays. *Magn Reson Med* 1997;38(5):852-857.
25. Nekolla S, Gneiting T, Syha J, Deichmann R, Haase A. T1 maps by K-space reduced snapshot-FLASH MRI. *J Comput Assist Tomogr* 1992;16(2):327-332.

26. Ou X, Gochberg DF. MT effects and T1 quantification in single-slice spoiled gradient echo imaging. *Magn Reson Med* 2008;59(4):835-845.
27. Deoni SC, Rutt BK, Jones DK. Investigating the effect of exchange and multicomponent T(1) relaxation on the short repetition time spoiled steady-state signal and the DESPOT1 T(1) quantification method. *J Magn Reson Imaging* 2007;25(3):570-578.
28. Bokacheva L, Huang AJ, Chen Q, Oesingmann N, Storey P, Rusinek H, Lee VS. Single breath-hold T1 measurement using low flip angle TrueFISP. *Magn Reson Med* 2006;55(5):1186-1190.
29. Piechnik SK, Ferreira VM, Dall'Armellina E, Cochlin LE, Greiser A, Neubauer S, Robson MD. Shortened Modified Look-Locker Inversion recovery (ShMOLLI) for clinical myocardial T1-mapping at 1.5 and 3 T within a 9 heartbeat breathhold. *J Cardiovasc Magn Reson*;12:69.
30. Stanisz GJ, Odrobina EE, Pun J, Escaravage M, Graham SJ, Bronskill MJ, Henkelman RM. T1, T2 relaxation and magnetization transfer in tissue at 3T. *Magn Reson Med* 2005;54(3):507-512.
31. Gold GE, Han E, Stainsby J, Wright G, Brittain J, Beaulieu C. Musculoskeletal MRI at 3.0 T: relaxation times and image contrast. *Ajr* 2004;183(2):343-351.

32. Scheffler K. 2003. ISMRM Proceedings 552.

## CHAPTER 4

### 4 ERROR ANALYSIS IN MOLLI CARDIAC $T_1$ MAPPING<sup>2</sup>

#### 4.1 Abstract

$T_1$  mapping is a promising quantitative tool for assessing diffuse cardiomyopathies. The purpose of this study is to quantify in vivo accuracy of the Modified Look-Locker Inversion Recovery (MOLLI) cardiac  $T_1$  mapping sequence against the spin echo gold standard, which has not been done previously.  $T_1$  accuracy of MOLLI was determined by comparing with the gold standard inversion recovery spin echo sequence in the calf muscle, and with a rapid inversion recovery fast spin echo sequence in the heart.  $T_1$  values were obtained with both conventional MOLLI fitting and MOLLI fitting with inversion efficiency correction. In the calf (n=6), conventional MOLLI fitting produced inconsistent  $T_1$  values with error ranging from 8.0% at 90° to 17.3% at 30°. Modified MOLLI fitting with inversion efficiency correction improved error to under 7.4% at all flip angles. In the heart (n=5), modified MOLLI fitting with inversion correction reduced  $T_1$  error to 5.5% from 14.0% by conventional MOLLI fitting. This study shows that conventional MOLLI fitting can lead to significant in vivo  $T_1$  errors when not accounting for the lower adiabatic inversion efficiency often experienced in vivo.

---

<sup>2</sup> Accepted for publication: Cooper MA, Nguyen TD, Spincemaille P, Prince MR, Weinsaft JW, Wang Y. (2014) How Accurate is MOLLI  $T_1$  Mapping In Vivo? Validation by Spin Echo Methods. PLOS One.

## 4.2 Introduction

$T_1$  mapping is a tissue characterization technique that uses measurements of the  $T_1$  relaxation time in the heart to quantify disease. Recently,  $T_1$  mapping has applied to a broad range of applications including lipid or iron deposition in the myocardium, pathological changes due to edema (1). In addition,  $T_1$  mapping shows promise for assessing cardiac amyloidosis (2-4) and cardiomyopathies that result in diffuse myocardial fibrosis (5-9). The MOLLI (Modified Look Locker Inversion Recovery) sequence (10) is a fast 2D inversion recovery (IR) balanced steady-state free precession (bSSFP) based  $T_1$  mapping method for cardiac imaging that is increasingly being used to probe differences between healthy and diseased states in the myocardium. While the accuracy of MOLLI has been studied extensively using computer simulations and water phantoms (10-13), a direct comparison of MOLLI with the gold standard IR spin echo (IR-SE) method has not yet been performed in vivo, where tissues may behave differently from water phantoms. This work aims to quantify MOLLI accuracy in vivo by comparing with the accurate but time-consuming gold standard IR-SE sequence in the calf muscle and with a rapid IR fast spin echo (IR-FSE) sequence in the heart of healthy volunteers. In addition, we quantified the effect of correcting for imperfect inversion efficiency (13-15) on the  $T_1$  accuracy of MOLLI.

## 4.3 Material and Methods

### *4.3.1 T<sub>1</sub> Fitting Approaches for MOLLI Data*

The MOLLI sequence consists of inversion pulses followed by mixed periods of bSSFP readout and free relaxation and therefore has a fairly complex signal evolution (Fig.4.1). To overcome this problem, previous T<sub>1</sub> mapping studies using MOLLI typically approximated this signal curve using a mono-exponential fit to extract an apparent T<sub>1</sub> relaxation time (T<sub>1</sub>\*) and subsequently corrected it to yield an improved T<sub>1</sub> estimate (10):

$$T_1 \approx T_1^* (B/A - 1) \quad [4.1]$$

where T<sub>1</sub>\* (the apparent T<sub>1</sub> relaxation), A and B are obtained by a three-parameter exponential fit of the MOLLI data (after restoring signal polarity and rearranging data according to their inversion times). While simple, this correction was originally derived for T<sub>1</sub> mapping with IR spoiled gradient echo (SPGR) Look-Locker imaging with continuous readouts (13,16) and therefore is not directly applicable to IR-bSSFP *modified* Look-Locker imaging with mixed readout and free relaxation periods. As a result, the correction in Eq. 4.1 is known to deliver accurate T<sub>1</sub> estimates only for certain T<sub>1</sub>/T<sub>2</sub> values and flip angles (11-13).

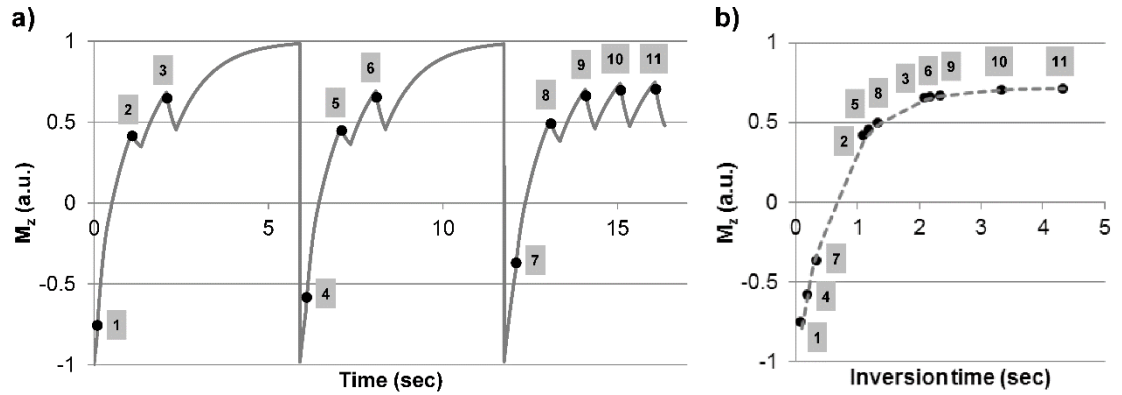


**Figure 4.1:** A) Simulated behavior of the longitudinal magnetization during MOLLI acquisition ( $T_1 = 1000$  ms,  $T_2 = 30$  ms, readout flip angle =  $30^\circ$ , echo train length = 64, heart rate = 60 bpm). Note the complex pattern of the underlying magnetization evolution due to mixed periods of bSSFP readout and free relaxation. MOLLI data are sampled at 11 inversion times marked in red. B) Conventional MOLLI fitting approximates the rearranged MOLLI data with a mono-exponential function to derive an apparent  $T_1$ , which is then corrected according to Eq. 4.1.

In addition to not fully accounting for complex MOLLI signal evolution (Fig. 4.1), Eq. 4.1 assumes perfect inversion efficiency (i.e., 100% of the longitudinal magnetization is inverted by the inversion pulse) (13-15). Typically, long adiabatic inversion pulses (e.g., the hyperbolic secant pulse is approximately 8 ms on our system) are favored over short hard inversion pulses to provide uniform inversion in the presence of  $B_0$  and  $B_1$  field inhomogeneities in vivo (10,17). These adiabatic pulses can introduce non-negligible  $T_2$  induced signal loss in tissues with shorter  $T_2$  relaxation times such as muscle and myocardium. It is possible to account for this

error when the inversion efficiency is known. Reference (15) derived the following equation from Eq.4.1 to include inversion efficiency:

$$T_1 \approx T_1^* (B/A - 1)/\delta \quad [4.2]$$

where  $\delta$  is the measured inversion efficiency. However, to our knowledge this has only been tested in phantoms (15) and has yet to be demonstrated in vivo. In this work, the inversion efficiency was obtained as a by-product of the T1 fitting of the gold-standard IR-SE data and used in the fitting of MOLLI data.

#### *4.3.2 Imaging Experiments*

All experiments were performed on a 1.5T GE HDxt MRI scanner (GE Healthcare, Waukesha, WI) using an 8-channel receiver coil (GE Healthcare Coils, Aurora, OH). The study was approved by the Weill Cornell Institutional Review Board and all healthy volunteers provided written informed consent prior to imaging. Due to the length of the MRI study in the calf, healthy volunteers were enrolled in two separate groups for the calf and cardiac imaging experiments (one volunteer participated in both experiments). A 2D IR-SSFP MOLLI sequence was implemented following the method described in (10). An 8.12 ms hyperbolic secant adiabatic inversion pulse and a 0.5 ms apodized half-sinc SSFP excitation pulse were used for all experiments.

MOLLI data was acquired in the calf muscle of 6 volunteers (5 men, 1 woman, mean age  $30 \pm 6$  years). Calf muscle was chosen for in vivo validation since its MR relaxation properties ( $T_1/T_2 \sim 1000/30$  ms) are similar to that of myocardium ( $T_1/T_2 \sim 1100/50$  ms). Imaging the calf muscle also eliminates the confounding effects of

motion and heart rate variability on the  $T_1$  accuracy of MOLLI (18,19), as well as enables the acquisition of the time-consuming gold standard IR-SE data, which is impractical in the heart. Typical MOLLI imaging parameters were as follows: TR = 4.1 ms, TE = 1.2 ms (asymmetric echo), matrix = 256x128 (interpolated to 256x256), FOV = 26-30 cm, partial FOV factor = 0.5, 11 inversion times (TI) = 100, 200, 350, 100+RR, 200+RR, 350+RR, 100+2RR, 200+2RR, 350+2RR, 350+3RR, 350+4RR (RR = cardiac interval). A 3 sec free relaxation period was introduced between subsequent modified Look-Locker experiments similar to that used in the original MOLLI sequence (10). A 6 Kaiser-Bessel RF ramp (20) was used to prepare magnetization prior to SSFP data acquisition. MOLLI data were acquired with 30°, 60° and 90° readout flip angles. 2D IR-SE reference data was acquired with the following imaging parameters: TR = 6 sec, TE = 10 ms, matrix = 256x128 (interpolated to 256x256), partial FOV factor = 0.5, TI = 20, 300, 1000 ms and  $\infty$ , scan time = 26 min. Synthetic gating incorporated in the scanner software was used to avoid variations in the cardiac R-R interval (BPM = 80).

Cardiac MOLLI data were acquired in 5 healthy volunteers (5 men, mean age  $36 \pm 11$  years) with peripheral gating and imaging parameters similar to that reported in (11,21): TR = 3.3 ms, TE = 0.9 ms (asymmetric echo), flip angle = 30°, FOV = 35-36 cm, partial FOV factor = 0.75, parallel imaging (ASSET) factor R = 2, 11 TIs, 3 heartbeat pause between subsequent modified Look-Locker experiments, scan time = 17 heartbeats. Since the gold standard IR-SE sequence is too time-consuming for cardiac applications, a rapid cardiac gated single-shot IR-FSE sequence with variable

refocusing flip angles was implemented to obtain reference myocardial  $T_1$  within one breath-hold (22). The typical IR-FSE imaging parameters were as follows: TR = 5 RR, minimum TE = 4 ms, echo train length = 48, matrix = 256x128, partial FOV factor = 0.75, TI = 20, 300, 1000 ms and  $\infty$ , ASSET factor R = 2, scan time = 16 heartbeats. Before use as a reference in the heart, the accuracy of the IR-FSE sequence was verified against the gold standard IR-SE in the calf muscle.

#### *4.3.3 Data Analysis*

All data were processed using Matlab R2009a (The Mathworks, Natick, MA) on a Dell XPS 8100 desktop computer. The polarity of the sampled data was restored using the method proposed in (23). IR-SE data were fit using a three-parameter exponential signal equation  $A - B\exp(-TI/T_1)$  to obtain the reference  $T_1$  and inversion efficiency ( $\delta = B/A - 1$ ). MOLLI data were fit using both conventional MOLLI fitting (Eq. 4.1) and MOLLI fitting corrected with known inversion efficiency (Eq. 4.2). Eq. 4.2 used the inversion efficiency  $g$  obtained from IR-SE acquisition.

In the calf, signals were averaged within a 3x3 region of interest (ROI) placed in the right soleus muscle of each volunteer prior to data fitting. There were no repeated measurements in the left and right calf muscles of the volunteers. For cardiac imaging, pixel-wise fitting was performed for an ROI placed in the left ventricular septum wall. IR-FSE data were processed using a three-parameter exponential fit to obtain the reference  $T_1$ .

Ideally one needs to perform mapping of inversion efficiency in the heart in order to accurately correct for myocardial T<sub>1</sub> obtained by MOLLI. Because this by itself is a difficult problem (e.g., due to respiratory and cardiac motion), a partial solution is offered by mapping the inversion efficiency in the calf muscle and then adjusting this value for the heart muscle based on the theoretical difference predicted by Bloch simulation while accounting for expected values of T<sub>1</sub> and T<sub>2</sub> in the myocardium (see Results section). While this approach is not viable clinically, it allows for the demonstration of the improved T<sub>1</sub> accuracy that can be obtained in the heart with inversion efficiency correction.

$$\text{Relative T}_1 \text{ error} \left| \frac{T_{1,MOLLI} - T_{1,IRSE}}{T_{1,IRSE}} \right| \times 100 \text{ and relative fitting residual } \frac{\|S_{measured} - S_{fitted}\|_2}{\|S_{measured}\|_2}$$

x100 were calculated, and statistical significance of the difference between the mean measured T<sub>1</sub> and the mean T<sub>1</sub> from IR-SE/FSE (gold standard) was determined using a one-way analysis of variance (ANOVA) test followed by the Tukey-Kramer method (multcompare function in Matlab 2014). A P-value of less than 0.05 was considered statistically significant.

#### 4.4 Results

In the calf muscle (n=6), conventional MOLLI fitting (Eq. 4.1) produced fairly inaccurate and inconsistent T<sub>1</sub> values as the readout flip angle was varied, with average T<sub>1</sub> error reaching as high as 17.3% at 30° (Fig. 4.2a/Table 4.1). Interestingly, T<sub>1</sub> error by conventional MOLLI fitting was lower at higher flip angles (reducing to

8.0% at 90°) although the relative fitting residual increased markedly (Fig. 4.2b), from 3.7% at 30° (indicating a reasonable fit of the 3-parameter exponential model) to 11.8% at 90° (indicating a rather poor fit as shown in Fig. 4.2b/c). Using MOLLI fitting accounting for the inversion efficiency (Eq. 4.2), error was improved to be less than 7.4% at all flip angles.

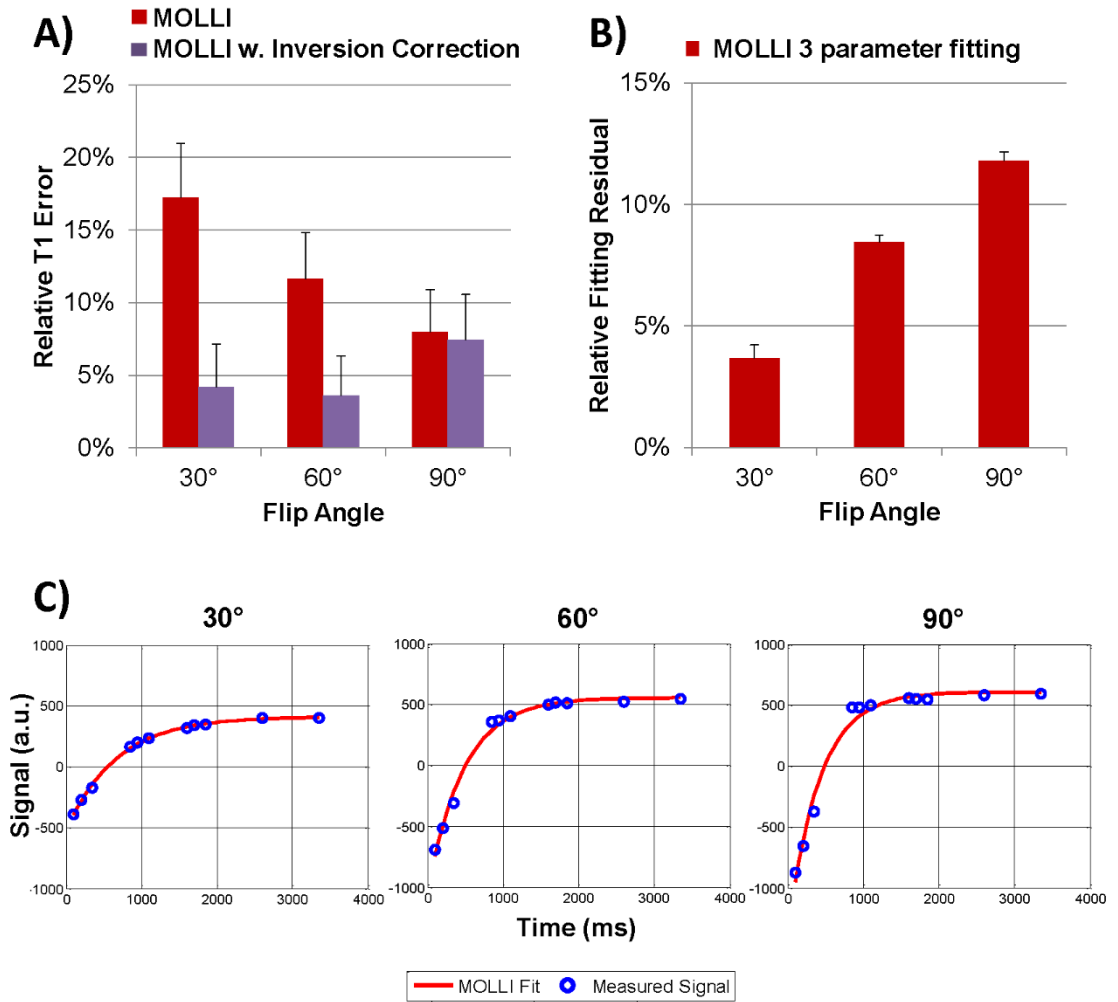


Figure 4.2: A) T1 errors obtained at 30°, 60° and 90° readout flip angle in the calf muscle ( $n=6$ ) for conventional MOLLI fitting (Eq. 4.1) and MOLLI fitting with inversion correction (Eq. 4.2).

B). Relative fitting residuals for the three parameter fit used in Eqs. 4.1 and 4.2. Note the increasing residuals with the three parameter fitting (used by Eqs. 4.1 and 4.2) at higher flip angles.

C) Measured signal and curves fit with the 3-parameter MOLLI fit in the calf muscle of one volunteer at 30°, 60° and 90°. Notice the increasing discrepancy between the fit and measured data at higher flip angle, confirmed by the increase in fitting residual in (B).

Figure 4.3 shows an example of T<sub>1</sub> maps obtained in the calf muscle at 30°. The average inversion efficiency  $\eta$  obtained from IR-SE and used in MOLLI data fitting was  $85.7 \pm 1.6\%$ . The average fitting time per pixel was 0.03 s for three-parameter MOLLI fitting, assuming that the polarity of the signal curve had already been restored.

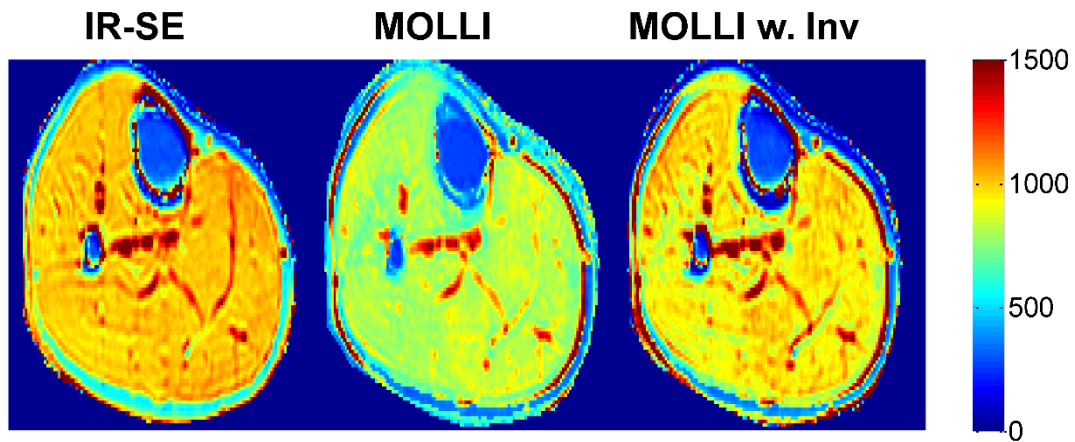


Figure 4.3. Example of T<sub>1</sub> maps (in ms) obtained with IR-SE, conventional MOLLI fitting and MOLLI fitting with inversion correction in the calf muscle at 30° flip angle.

In the calf muscle, the gold standard IR-SE and rapid IR-FSE acquisitions were found to provide similar T<sub>1</sub> values ( $1.3 \pm 0.7\%$  relative error;  $p=1$ ). However, the inversion efficiency measured by IR-FSE ( $81.9 \pm 2.0\%$ ) underestimated that obtained by IR-SE ( $85.7 \pm 1.6\%$ )  $p=0.002$ . To determine the in vivo inversion efficiency in the myocardium required for MOLLI data fitting, the theoretical inversion efficiency was simulated using T<sub>1</sub>/T<sub>2</sub> of healthy soleus muscle (985/31 ms) (24) and myocardium (1088/52 ms) (22,25) and the shape of the adiabatic pulse used in the imaging

experiment. Since simulation may not perfectly predict the in vivo inversion efficiency (15), the ratio of the simulated inversion efficiencies was then used to scale the average inversion efficiency obtained from the calf muscle (85.7%), yielding an inversion efficiency estimate of 88% for fitting of the cardiac data.  $B_1$  and  $B_0$  effects were not considered when estimating the inversion efficiency since the hyperbolic secant adiabatic inversion pulse is expected to be robust against  $B_1$  and  $B_0$  inhomogeneity encountered in vivo at 1.5 T. For  $T_1$  and  $T_2$  similar to that of the calf and the myocardium, the inversion efficiency is expected to vary by only a few percent with  $\pm 25\%$  variation in RF amplitude and  $\pm 150$  Hz off-resonance range as shown in figure 4 of (15).

<b>Calf Muscle (n=6)</b>								
	FA = 30°			FA = 60°			FA = 90°	
	IR-SE	IR-FSE	MOLLI	MOLLI w. Inv	MOLLI	MOLLI w. Inv	MOLLI	MOLLI w. INV
T1 (ms)	986 ± 32	987 ± 42	815 ± 40	952 ± 38	871 ± 36	1016 ± 27	907 ± 35	1058 ± 27
Inv. Eff.	85.7 ± 1.6%	81.9 ± 2.0%	N/A					
p	N/A	1	<0.001	0.69	<0.001	0.79	0.007	0.02
Fitting residual			3.7 ± 0.6%		8.5 ± 0.3%		11.8 ± 0.36%	

<b>Myocardium (n=5)</b>			
	FA = 30°		
	IR-FSE	MOLLI	MOLLI w. Inv
T1 (ms)	1092 ± 64	937 ± 60	1065 ± 68
Inv. Eff.	88% (sim. from calf and Bloch)	N/A	
p	N/A	0.006	0.78
Fitting residual		5.3% ± 1.8%	

**Table 4.1.** Comparison of T1 values obtained in the calf muscle (n=6) and myocardium (n=5) of healthy volunteers using conventional MOLLI fitting (Eq.4.1) and MOLLI fitting with inversion correction (Eq.4.2) at various flip angles (FA). P values are given for comparison with the gold standard IR-SE method (calf) or IR-FSE method (myocardium).

In the heart (n=5), MOLLI with inversion correction ( $T_1 = 1065 \pm 68$  ms;  $p = 0.78$ ) reduced T1 error compared to conventional MOLLI fitting ( $T_1 = 937 \pm 60$  ms;  $p = .006$ ) when compared to the reference  $T_1$  values provided by IR-FSE ( $T_1 = 1092 \pm 64$  ms). Overall, the relative T1 error was  $14.0 \pm 6.6\%$  for conventional MOLLI fitting, and  $5.5 \pm 5.1\%$  for MOLLI with inversion efficiency correction, closely following the trend observed in the calf experiments. A comparison of short-axis myocardial  $T_1$  maps obtained with the two MOLLI data fitting methods is shown in Fig. 4.4. The average heart rate was  $52.8 \pm 9.6$  bpm (range 40-63 bpm).

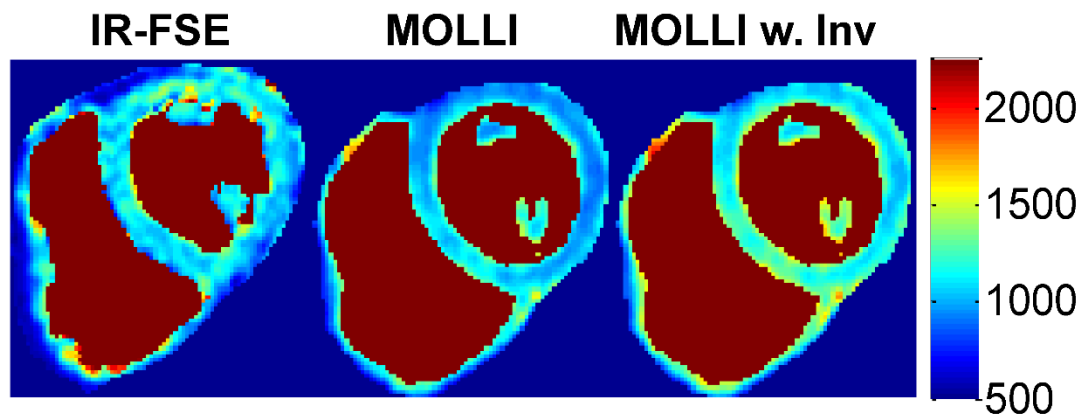


*Figure 4.4. Example of myocardial  $T_1$  maps (in ms) obtained with IR-FSE, conventional MOLLI fitting and MOLLI fitting with inversion correction at a  $30^\circ$  flip angle. The IR-FSE image was taken in a separate breath-hold than the MOLLI and therefore it is at a slightly different position. Blood has been segmented out to minimize distraction due to the blood  $T_1$ : IR-FSE spoils the blood signal and is not able to fit for blood  $T_1$ , however MOLLI is able to fit for  $T_1$  in the blood.*

#### 4.5 Discussion

Our in vivo data showed that conventional MOLLI (Eq. 4.1) provided fairly inaccurate and inconsistent in vivo  $T_1$  values in muscle tissues when compared with the standard spin echo based methods. As indicated by our results, a major source of  $T_1$  error comes from reduced adiabatic inversion efficiency due to shorter  $T_2$  of muscle tissues ( $T_1/T_2$  ratio  $\sim 30$ ). The correction for apparent  $T_1$  used in the conventional MOLLI fitting was originally derived for SPGR Look-Locker imaging assuming 100% inversion efficiency and therefore may not be adequate for describing a more complicated bSSFP signal evolution in MOLLI (Fig. 4.1), especially at reduced inversion efficiency. Limitations of the model are shown in Fig. 4.2 when imaging at higher flip angles causes larger fitting residuals. When accounting for the inversion efficiency in conventional MOLLI fitting (Eq.4. 2),  $T_1$  error was greatly reduced. The current work shows that conventional fitting after inversion efficiency correction (Eq. 4.2) is valid, even though, strictly speaking, it only applies to spoiled gradient echo based Look-Locker acquisitions (13,16). This finding agrees well with recent results obtained with an SPGR based MOLLI sequence at 7T (14) and serves to confirm that a source of error with traditional MOLLI  $T_1$  mapping is the inversion efficiency, which can be improved upon when using Eq. 4.2 if the inversion efficiency is measured. Further in vivo studies may be warranted to quantify  $T_1$  error in MOLLI as a function of inversion efficiency in different tissues.

The conventional MOLLI fitting method (Eq.4.1) has been validated in water phantoms doped with various contrast agents (10-12,18) by comparing with the gold

standard IR-SE method. However, water phantoms are different from in vivo tissue in biochemical composition and underlying biophysical process (e.g., exchange among water compartments), resulting in different relaxation and MRI signal behavior. In vivo validation of MOLLI has not been performed so far most likely due to the excessive IR-SE acquisition time. In this work, we used the calf muscle as a tissue model for the myocardium, thus enabling for the first time a direct in vivo comparison of MOLLI with IR-SE. For cardiac  $T_1$  mapping, a more rapid IR-FSE sequence was developed to enable cardiac  $T_1$  mapping in a single breath-hold (22). While conventional MOLLI fitting of phantom data traditionally shows good to excellent  $T_1$  accuracy (10-12,18), we found larger in vivo  $T_1$  errors (above 10%) in both the calf muscle and the myocardium which could be reduced to less than 7.4% when accounting for inversion efficiency as in Eq. 4.2. This observation suggests that in vivo validation should be considered following the initial phantom validation when assessing the performance of  $T_1$  mapping for in vivo imaging.

Our in vivo  $T_1$  results obtained with the conventional MOLLI fitting (Eq. 4.1) are similar to that reported in previous studies (761 ms in the skeletal muscle (10) and 962-998 ms in the myocardium (10,18,21)). Interestingly, we observed increasing  $T_1$  values at higher readout flip angles in the calf muscle, a trend opposite to that reported previously in the myocardium (11). To better understand this phenomenon, we have performed Bloch simulation for  $T_1/T_2$  of the calf muscle and the heart and observed that the trend highly depends on tissue  $T_2$  and other timing parameters such as heart rate. In addition, conventional MOLLI analysis (Eq. 4.1) does not explicitly take into

account the flip angle, since it was originally derived for SPGR imaging, and as a result can provide a flip angle dependent bias specific to tissue T1/T2. This bias may explain the increase in T1 error after inversion efficiency correction, especially at higher flip angles of 60° and 90°. This is additional evidence that the conventional MOLLI data fitting may not work well for different tissues or when imaging conditions are changed.

The above findings are significant for two reasons. First, inversion efficiency correction can significantly reduce T<sub>1</sub> error in MOLLI to within 7.4%, thereby improving the reliability of this technique for diagnostic purposes. Second, the improved consistency of T<sub>1</sub> estimates at different flip angles and T<sub>1</sub>/T<sub>2</sub> values after applying correction (Eq. 4.2) to MOLLI analysis may benefit multi-site multi-vendor T<sub>1</sub> mapping studies by reducing discrepancies due to different hardware and software implementations.

This work has several limitations. The effect of inversion efficiency on T<sub>1</sub> fitting post contrast, which is important for clinical application, was not investigated. This was because myocardial T<sub>1</sub> can vary significantly post contrast depending on factors such as cardiac output and bolus timing, making accurate comparisons between the reference IR-FSE sequence and the MOLLI sequence in multiple subjects challenging. The long echo train of the IR-FSE sequence may also result in errors due to blurring in tissue with short T<sub>1</sub>. The trade-off between scan time reduction by prolonging the echo train (which is relevant for breath-hold cardiac imaging) and the associated image

blurring in such situations is an important question and will be investigated in our future work. In addition, post-contrast myocardial  $T_2$  is difficult to measure for the same reason, making the estimation of inversion efficiency non-trivial. In this work, in vivo inversion efficiency was obtained as a by-product of IR-SE data fitting, which is not a practical method due to long IR-SE acquisition time and the lack of experimental mapping of in vivo inversion efficiency in the heart further limited the work.

A fitting method that can improve MOLLI  $T_1$  estimates in vivo using Eq. 4.2 would require the knowledge of imaging and tissue parameters (e.g., inversion efficiency), which may not be readily available. For the sake of analysis, in this paper, inversion efficiency obtained in the calf was scaled by Bloch simulation to obtain a theoretical inversion efficiency in the heart. The authors acknowledge that it is not clinically viable to perform an IR-SE scan of the calf in order to correct for the imperfect inversion efficiency in a subsequent MOLLI scan of the heart. The main contribution of this was to identify inversion efficiency as a major source of  $T_1$  error in MOLLI using a SE based method as a reference standard in vivo, which has not been done previously. Mapping inversion efficiency, however, is a non-trivial problem particularly in the in vivo setting, and this is an important limitation of the MOLLI approach. We believe that IR-FSE is a better approach in patients with lower heart rate (to reduce the motion sensitivity of the FSE readout) and when blood  $T_1$  is not needed. Another potential solution could be to fit for the inversion efficiency, however this requires the use of an SPGR readout with reduced SNR efficiency a four parameter fit that is more sensitive to noise (14). A shorter adiabatic pulse could also

be used to improve the inversion efficiency, although this is often limited by the maximum allowable RF transmit power (15).

Other potential factors limiting MOLLI accuracy in vivo, but not studied here, were reviewed in (13) and may include, but are not limited to deviation from the nominal flip angle profile (24,26), heart rate variability (18,27,28), magnetization transfer (MT) effect (26,29-31), motion (19), and  $B_0$  inhomogeneity (13,32). Recent works have proposed acquiring MT sensitive data (e.g., by varying RF pulse length) and including MT effect in the signal model (26,29,30) for accurate  $T_1$  fitting; however, the utility of this approach for cardiac  $T_1$  mapping using MOLLI remains to be investigated. A potential solution for these imperfections could be to develop a IR-FSE based  $T_1$  mapping sequence (22) which is more robust against imperfect inversion efficiency and field inhomogeneities than the bSSFP based MOLLI sequence.

In conclusion, the conventional correction (Eq. 4.1) of apparent  $T_1$  in MOLLI can lead to significant in vivo  $T_1$  errors partly due to lower adiabatic inversion efficiency in muscle tissues.  $T_1$  errors can be reduced significantly by using a modified version of the conventional MOLLI correction accounting for inversion efficiency (Eq. 4.2), when the inversion efficiency is known.

#### 4.6 References

1. Moon JC, Messroghli DR, Kellman P, Piechnik SK, Robson MD, Ugander M, Gatehouse PD, Arai AE, Friedrich MG, Neubauer S, Schulz-Menger J, Schelbert EB, Imaging SfCMR, Cardiology CMRWGotESo. Myocardial T1 mapping and extracellular volume quantification: a Society for Cardiovascular Magnetic Resonance (SCMR) and CMR Working Group of the European Society of Cardiology consensus statement. *J Cardiovasc Magn Reson* 2013;15:92.
2. Maceira AM, Joshi J, Prasad SK, Moon JC, Perugini E, Harding I, Sheppard MN, Poole-Wilson PA, Hawkins PN, Pennell DJ. Cardiovascular magnetic resonance in cardiac amyloidosis. *Circulation* 2005;111(2):186-193.
3. Maceira AM, Prasad SK, Hawkins PN, Roughton M, Pennell DJ. Cardiovascular magnetic resonance and prognosis in cardiac amyloidosis. *J Cardiovasc Magn Reson* 2008;10:54.
4. Krombach GA, Hahn C, Tomars M, Buecker A, Grawe A, Gunther RW, Kuhl HP. Cardiac amyloidosis: MR imaging findings and T1 quantification, comparison with control subjects. *J Magn Reson Imaging* 2007;25(6):1283-1287.
5. Sparrow P, Messroghli DR, Reid S, Ridgway JP, Bainbridge G, Sivananthan MU. Myocardial T1 mapping for detection of left ventricular myocardial fibrosis in

chronic aortic regurgitation: pilot study. *AJR Am J Roentgenol* 2006;187(6):W630-635.

6. Iles L, Pfluger H, Phrommintikul A, Cherayath J, Aksit P, Gupta SN, Kaye DM, Taylor AJ. Evaluation of diffuse myocardial fibrosis in heart failure with cardiac magnetic resonance contrast-enhanced T1 mapping. *J Am Coll Cardiol* 2008;52(19):1574-1580.

7. Sibley CT, Noureldin RA, Gai N, Nacif MS, Liu S, Turkbey EB, Mudd JO, van der Geest RJ, Lima JA, Halushka MK, Bluemke DA. T1 Mapping in cardiomyopathy at cardiac MR: comparison with endomyocardial biopsy. *Radiology* 2012;265(3):724-732.

8. Lu M, Zhao S, Yin G, Jiang S, Zhao T, Chen X, Tian L, Zhang Y, Wei Y, Liu Q, He Z, Xue H, An J, Shah S. T1 mapping for detection of left ventricular myocardial fibrosis in hypertrophic cardiomyopathy: a preliminary study. *Eur J Radiol* 2013;82(5):e225-231.

9. Broberg CS, Chugh SS, Conklin C, Sahn DJ, Jerosch-Herold M. Quantification of diffuse myocardial fibrosis and its association with myocardial dysfunction in congenital heart disease. *Circ Cardiovasc Imaging* 2010;3(6):727-734.

10. Messroghli DR, Radjenovic A, Kozerke S, Higgins DM, Sivananthan MU, Ridgway JP. Modified Look-Locker inversion recovery (MOLLI) for high-resolution T1 mapping of the heart. *Magn Reson Med* 2004;52(1):141-146.
11. Messroghli DR, Greiser A, Frohlich M, Dietz R, Schulz-Menger J. Optimization and validation of a fully-integrated pulse sequence for modified look-locker inversion-recovery (MOLLI) T1 mapping of the heart. *J Magn Reson Imaging* 2007;26(4):1081-1086.
12. Gai ND, Stehning C, Nacif M, Bluemke DA. Modified Look-Locker T1 evaluation using Bloch simulations: Human and phantom validation. *Magnetic Resonance in Medicine* 2013;69(2):329-336.
13. Kellman P, Hansen M. T1-mapping in the heart: accuracy and precision. *Journal of Cardiovascular Magnetic Resonance* 2014 Jan 4; doi: 10.1186/1532-429X-16-2 [Epub ahead of print].
14. Rodgers CT, Piechnik SK, Delabarre LJ, Van de Moortele PF, Snyder CJ, Neubauer S, Robson MD, Vaughan JT. Inversion recovery at 7 T in the human myocardium: Measurement of T(1) , inversion efficiency and B(1) (+). *Magn Reson Med* 2012.
15. Kellman P, Herzka DA, Hansen MS. Adiabatic inversion pulses for myocardial T1 mapping. *Magn Reson Med* 2014;71(4):1428-1434.

16. Deichmann R, Haase A. Quantification of T1 values by SNAPSHOT-FLASH NMR imaging. *Journal of Magnetic Resonance (1969)* 1992;96(3):608-612.
17. Kim D, Cernicanu A, Axel L. B(0) and B(1)-insensitive uniform T(1)-weighting for quantitative, first-pass myocardial perfusion magnetic resonance imaging. *Magn Reson Med* 2005;54(6):1423-1429.
18. Piechnik SK, Ferreira VM, Dall'Armellina E, Cochlin LE, Greiser A, Neubauer S, Robson MD. Shortened Modified Look-Locker Inversion recovery (ShMOLLI) for clinical myocardial T1-mapping at 1.5 and 3 T within a 9 heartbeat breathhold. *J Cardiovasc Magn Reson* 2010;12:69.
19. Xue H, Shah S, Greiser A, Guetter C, Littmann A, Jolly MP, Arai AE, Zuehlsdorff S, Guehring J, Kellman P. Motion correction for myocardial T1 mapping using image registration with synthetic image estimation. *Magn Reson Med* 2012;67(6):1644-1655.
20. Nguyen TD, Spincemaille P, Prince MR, Wang Y. Cardiac fat navigator-gated steady-state free precession 3D magnetic resonance angiography of coronary arteries. *Magn Reson Med* 2006;56(1):210-215.

21. Messroghli DR, Plein S, Higgins DM, Walters K, Jones TR, Ridgway JP, Sivananthan MU. Human myocardium: single-breath-hold MR T1 mapping with high spatial resolution--reproducibility study. *Radiology* 2006;238(3):1004-1012.
22. Nguyen TD, Cooper, M.A., Spincemaille, P. Weinsaft, J.W., Prince, M.R., Wang, Y. A new method for accurate myocardial T1 mapping using Variable Angle Long Echo train Relaxometric Imaging (VALERI). Proceedings of the 21st Annual Meeting ISMRM; 2013; Salt Lake City, UT. p 262. (Proceedings of the 21st Annual Meeting ISMRM).
23. Nekolla S, Gneiting T, Syha J, Deichmann R, Haase A. T1 maps by K-space reduced snapshot-FLASH MRI. *J Comput Assist Tomogr* 1992;16(2):327-332.
24. Cooper MA, Nguyen TD, Spincemaille P, Prince MR, Weinsaft JW, Wang Y. Flip angle profile correction for T(1) and T(2) quantification with look-locker inversion recovery 2D steady-state free precession imaging. *Magn Reson Med* 2012;68(5):1579-1585.
25. Giri S, Chung YC, Merchant A, Mihai G, Rajagopalan S, Raman SV, Simonetti OP. T2 quantification for improved detection of myocardial edema. *J Cardiovasc Magn Reson* 2009;11:56.

26. Ehses P, Seiberlich N, Ma D, Breuer FA, Jakob PM, Griswold MA, Gulani V. IR TrueFISP with a golden-ratio-based radial readout: fast quantification of T1, T2, and proton density. *Magn Reson Med* 2013;69(1):71-81.
27. Fitts M, Breton E, Kholmovski EG, Dossdall DJ, Vijayakumar S, Hong KP, Ranjan R, Marrouche NF, Axel L, Kim D. Arrhythmia insensitive rapid cardiac T1 mapping pulse sequence. *Magn Reson Med* 2013;70(5):1274-1282.
28. Weingartner S, Akcakaya M, Basha T, Kissinger KV, Goddu B, Berg S, Manning WJ, Nezafat R. Combined saturation/inversion recovery sequences for improved evaluation of scar and diffuse fibrosis in patients with arrhythmia or heart rate variability. *Magn Reson Med* 2013.
29. Gloor M, Scheffler K, Bieri O. Quantitative magnetization transfer imaging using balanced SSFP. *Magn Reson Med* 2008;60(3):691-700.
30. Gloor M, Scheffler K, Bieri O. Analytical description of magnetization transfer effects on the transient phase of balanced SSFP. *Proceedings of the 20th Annual Meeting ISMRM; 2012; Melbourne, Australia.* p 4262. (*Proceedings of the 20th Annual Meeting ISMRM*).
31. Robson MD, Piechnik SK, Tunnicliffe EM, Neubauer S. T measurements in the human myocardium: The effects of magnetization transfer on the SASHA and MOLLI sequences. *Magn Reson Med* 2013.

32. Kellman P, Herzka DA, Arai AE, Hansen MS. Influence of Off-resonance in myocardial T1-mapping using SSFP based MOLLI method. *J Cardiovasc Magn Reson* 2013;15:63.

## CHAPTER 5

### 5 T1 MAPPING OF CARDIAC AMYLOID

#### 5.1 Introduction

Cardiac amyloidosis is a non-ischemic cardiomyopathy in which insoluble proteins accumulate in the extracellular space of the myocardium, resulting in heart failure and death. The current gold standard for the diagnosis of cardiac amyloid is endomyocardial biopsy, an invasive procedure not well suited for screening purposes or serial assessment. Myocardial T1 mapping after the administration of gadolinium (Gd) contrast, which distributes within the myocardial extracellular space, has emerged as a noninvasive tool to detect and potentially quantify severity of cardiac amyloid (1-3). However, optimal imaging time points for maximizing post-contrast T1 differences between healthy and amyloid affected myocardium have not been established. The purpose of this study was to identify optimal T1 mapping time for amyloid diagnosis by performing numerical simulation of a tracer kinetic model as well as by measuring myocardial T1 at serial time points in healthy and amyloid positive patients.

#### 5.2 Methods

Numerical simulation of the myocardial Gd concentration time curve was performed using a tracer kinetic model proposed by Henrik et al (4). The arterial input function was simulated using the local density random walk (LDRW) model with input parameters reported previously (5). Normal and diseased ECV was assumed to be 0.26 and 0.5 (3).

The cardiac MRI protocol (1.5 T) included 2 components – CINE imaging (SSFP) for cardiac structure/function, and T1 mapping for myocardial tissue characterization. T1 mapping was performed in two groups: 1 “amyloid +” subjects, defined by biopsy-proven systemic amyloid with associated remodeling suggestive of cardiac involvement (left ventricular [LV] hypertrophy and/or atrial dilation); 2 normative controls without risk factors for amyloid or cardiovascular disease. 13 subjects (6 amyloid +, 7 controls) were studied; all amyloid affected subjects had biopsy-confirmed systemic disease with associated remodeling suggestive of cardiac involvement. T1 mapping was done using a conventional modified Look-Locker inversion recovery (MOLLI) sequence (flip angle = 30°; matrix 256x128; parallel imaging reduction factor = 1.5; linear view ordering; 6 Kaiser-Bessel ramp preparation; 17 heart beat acquisition), with T1 calculated using an established formula ( $T1 = T1^* (B/A-1)$ , where  $T1^*$ , A, and B were obtained via three-parameter exponential fit). [Gd] was determined using  $1/T1,POST = 1/T1,PRE + R*[Gd]$  where the T1 relaxivity  $R = 4.3/\text{sec}/\text{mM}$  (4). To evaluate time-dependent differences in myocardial T1, MOLLI was acquired at sequential time points: pre-contrast (for concentration determination) and 3, 5, 10, 14, 20 minutes following intravenous administration of Gd (0.2 mmol/kg). T1 ROI analysis was performed for all subjects in the septal wall of the LV.

### 5.3 Results

Simulation predicted a peak difference in myocardial [Gd] between healthy and amyloid myocardium at approximately 1.5 min post contrast (Fig.5.1).

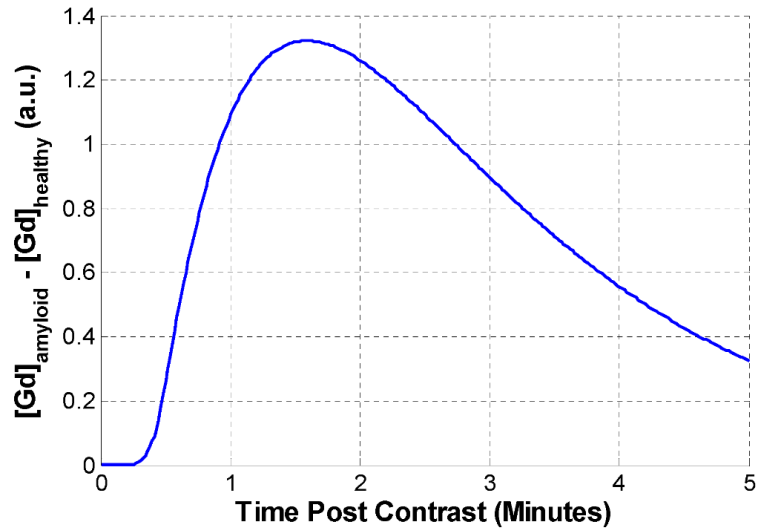


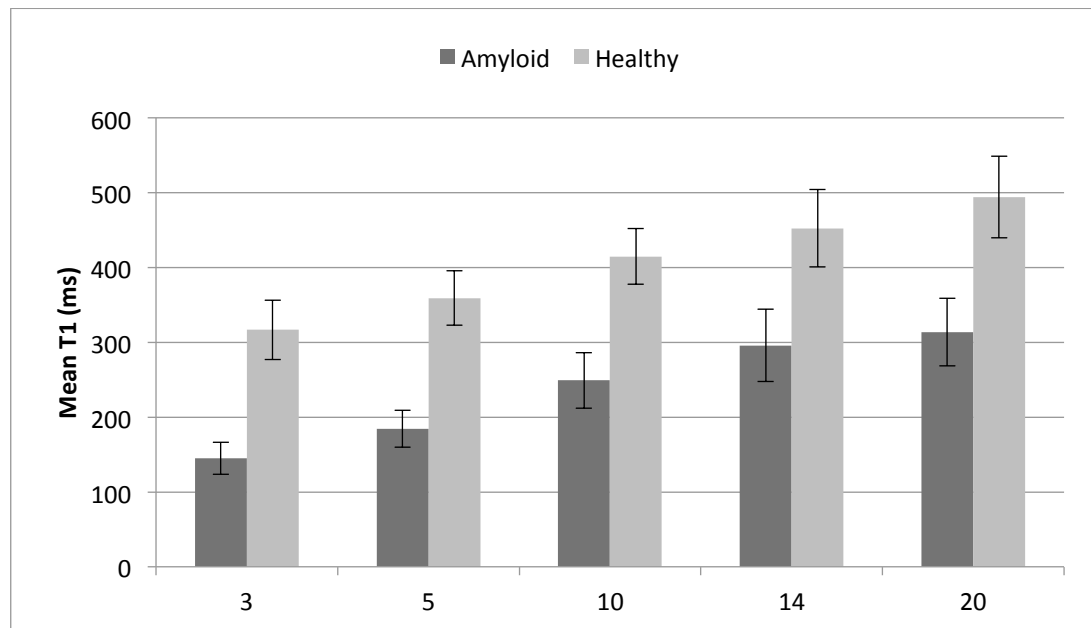
Figure 5.1: Simulation of the difference in myocardial [Gd] between healthy and amyloid myocardium.

Table 5.1 summarizes the functional cardiac measurements between the two imaging groups. Amyloid subjects had higher LV mass, lower myocardial contraction fraction and stroke volume, and larger left atrial area than controls, but similar LV end-diastolic volume, and LVEF.

	Amyloid (n=6)	Healthy (n=7)	P value
LV mass [gm]	185 ± 47	107 ± 42	<0.01
Contraction fraction	0.32 ± 0.07	0.85 ± 0.22	<0.001
Left atrial area [cm <sup>2</sup> ]	24 ± 6	18 ± 4	0.05
LV end-diastolic volume [ml]	111 ± 31	137 ± 41	0.24
LV stroke volume [ml]	62 ± 14	90 ± 28	0.05
LV ejection fraction [%]	57 ± 10	66 ± 4	0.1

Table 5.1: Functional cardiac parameters for healthy controls and amyloid subjects.

MOLLI was successfully acquired in all subjects at each time point: T1 differed significantly (all  $p \leq 0.05$ ) between amyloid and control groups at all times (Fig. 5.2).



However, concentration difference decreased following gadolinium administration (Fig. 5.3): T1 concentration differences between patients and controls were maximal at 3 minutes post-contrast with progressive decrements thereafter. Results in vivo were

comparable to the model shown in Fig. 5.1. Figure 5.4 shows T1 maps a different time points post contrast for one healthy control and one amyloid patient.

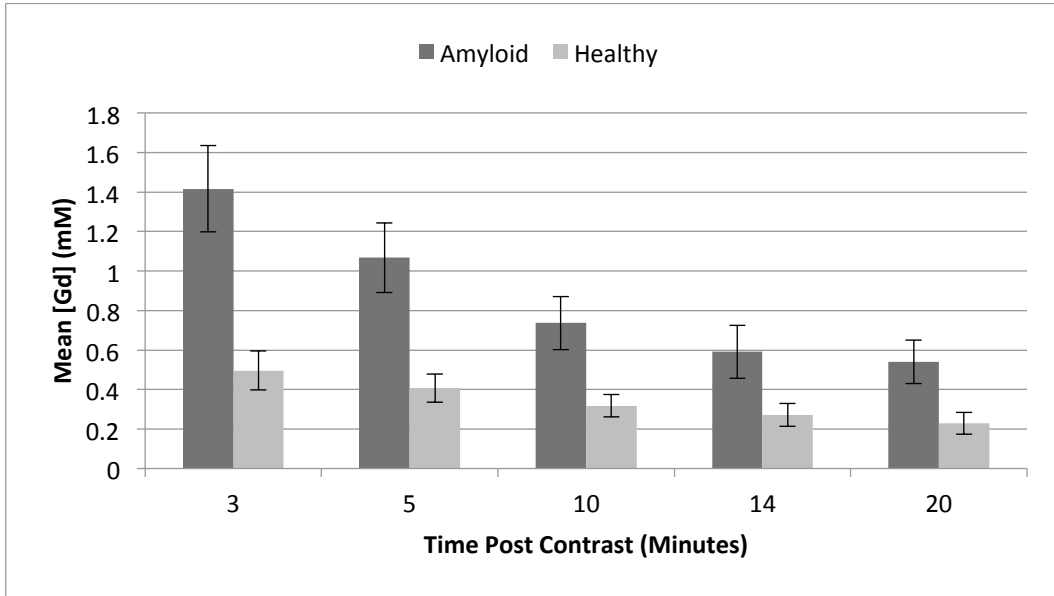


Figure 5.3: Mean concentrations for ROI analysis in healthy and amyloid cohorts.

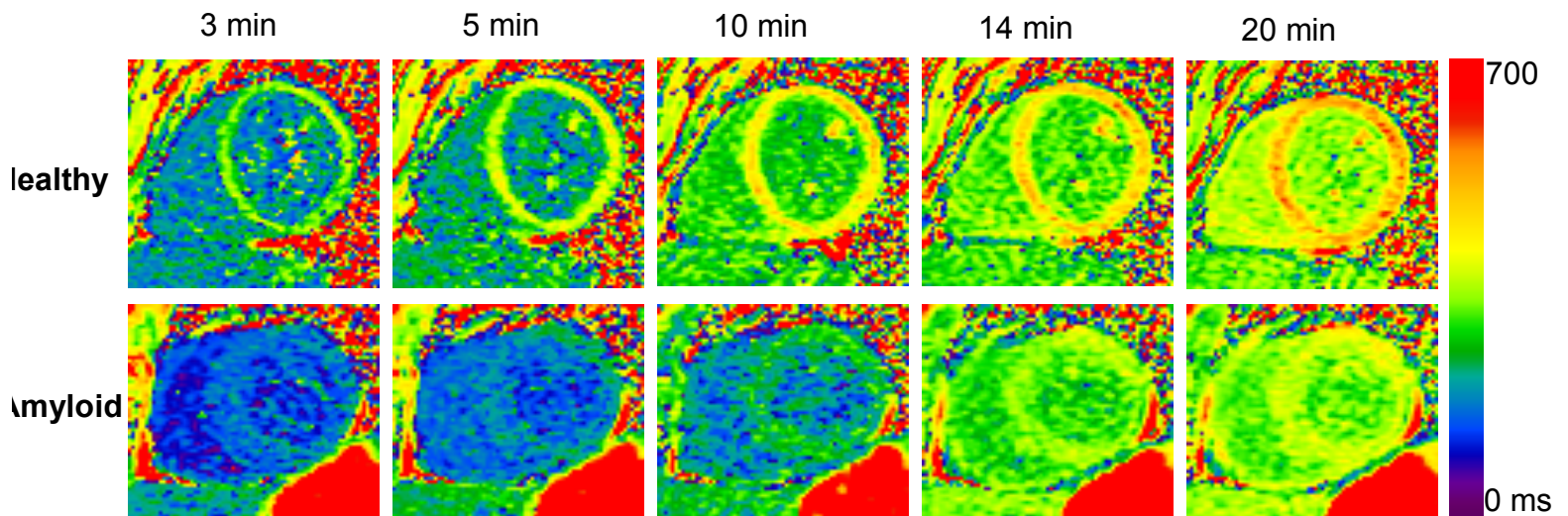


Figure 5.4: T1 maps for a healthy control and amyloid patient post contrast.

#### 5.4 Discussion

MOLLI-quantified myocardial T1 yields maximal difference between amyloid-affected subjects and normative controls within 3 minutes following gadolinium administration. Current findings support use of early post-contrast MOLLI T1 mapping for identification of cardiac amyloid.

## 5.5 References

1. Maceira AM, Joshi J, Prasad SK, Moon JC, Perugini E, Harding I, Sheppard MN, Poole-Wilson PA, Hawkins PN, Pennell DJ. Cardiovascular magnetic resonance in cardiac amyloidosis. *Circulation* 2005;111(2):186-193.
2. Robbers LF, Baars EN, Brouwer WP, Beek AM, Hofman MB, Niessen HW, van Rossum AC, Marcu CB. T1 mapping shows increased extracellular matrix size in the myocardium due to amyloid depositions. *Circ Cardiovasc Imaging* 2012;5(3):423-426.
3. Fontana M, White SK, Banypersad SM, Sado DM, Maestrini V, Flett AS, Piechnik SK, Neubauer S, Roberts N, Moon JC. Comparison of T1 mapping techniques for ECV quantification. Histological validation and reproducibility of ShMOLLI versus multibreath-hold T1 quantification equilibrium contrast CMR. *J Cardiovasc Magn Reson* 2012;14:88.
4. Larsson HB, Fritz-Hansen T, Rostrup E, Søndergaard L, Ring P, Henriksen O. Myocardial perfusion modeling using MRI. *Magn Reson Med* 1996;35(5):716-726.
5. de Rochefort L, Nguyen T, Brown R, Spincemaille P, Choi G, Weinsaft J, Prince MR, Wang Y. In vivo quantification of contrast agent concentration using the induced magnetic field for time-resolved arterial input function measurement with MRI. *Med Phys* 2008;35(12):5328-5339.

6. Messroghli DR, Radjenovic A, Kozerke S, Higgins DM, Sivanathan MU, Ridgway JP. Modified Look-Locker inversion recovery (MOLLI) for high-resolution T1 mapping of the heart. *Magn Reson Med* 2004;52(1):141-146.

## CHAPTER 6

### 6 ACCELERATED CARDIAC IMAGING

#### 6.1 Introduction

Spatial and temporal prior information has been increasingly explored for accelerating time resolved imaging. Previously, kt-GRAPPA and other methods (1-3) exploit temporal redundancy, but are restricted to strict Cartesian sampling or calibration kernels with specific patterns. kt-SPARSE, kt-FOCUSS and kt-SPIRiT (4-6) allow for arbitrary sampling while constraining temporal sparsity in an L1 sense, which may not always be optimal if the signal is not highly compressible. Here we propose PROST (Parallel Reconstruction Observing Self consistency and Temporal smoothness) which is implemented by extending the SPIRiT self-consistency kernel to the time domain enforcing temporal smoothness in k-t space while allowing arbitrary view ordering as in the original SPIRiT formulation (7).

#### 6.2 Theory

PROST is based on the assumption that each temporal phase has small changes with respect to its neighbors (temporal smoothness). To incorporate temporal smoothness, a spatial and temporal kernel (figure 6.1) is calibrated from training data that is acquired at each time point. Principal components analysis (PCA) is incorporated into PROST to further express the information redundancy in the temporal dimension thereby reducing the number of unknowns (8,9). PROST can be formulated as a least squares minimization:

$$\operatorname{argmin}_x \|DBx - y\|^2 + \lambda \|(G - I)Bx\|^2 \quad [6.1]$$

Where  $y$  is the sampled data in  $k$ -space and all time and  $Bx$  is the reconstructed  $k$ -space data over all time.  $G$  is the grappa kernel, which extends over the  $k$ -space, the coil as well as the time dimension (figure 6.1).  $D$  is a projection onto the acquired  $k$ -space lines,  $B$  is the temporal basis derived from a principal components analysis of the fully acquired center of  $k$ -space and  $x$  are the unknown spatial weights of the  $k$ -space data in the  $B$  basis. The conjugate gradient algorithm was used to solve the minimization problem.

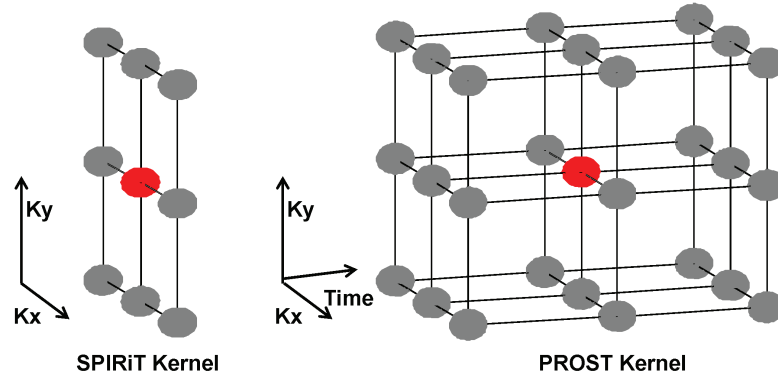


Figure 6.1: The standard SPIRiT kernel and the spatio-temporal SPIRiT kernel used in PROST. The red sphere is fit using neighbors (grey) in  $k$ -space (SPIRiT) and both  $k$ -space and time (PROST). For simplicity, the coil dimension is not shown.

### 6.3 Methods

Optimization was carried out on a retrospectively under-sampled CINE scan by varying the number of training lines, number of principal components and kernel sizes. After optimization, a pulse sequence was developed to implement a truly under-sampled data acquisition with semi-random Cartesian golden ratio view ordering. 8 healthy volunteers were scanned at 1.5 T. CINE imaging was carried out at 1x under-sampling and 6x (true) under-sampling including 6 training lines for PCA and kernel calibration. Scan parameters were: 256x192 matrix, .75 PFOV, 1 NEX, 8 views per segment (VPS) and 12-14 slices (6 mm thick; 4 mm gap).

Scan times varied based on heart rates. The 6x under-sampled scan required 3-4 breath-holds for whole heart coverage compared to 12-14 breath-holds (depending on the number of slices) for fully sampled reference scans. MATLAB (Mathworks, Natick MA) was used for reconstruction. Ejection fraction was determined by an experienced reader.

### 6.4 Results

Optimal parameters were as follows: [3x3x3] kernel size, 10 principal components and 6 training lines. These parameters were used for comparison of PROST, PROST without PCA and SPIRiT using temporal updates as in (7) on a retrospectively under-sampled dataset (figure 5.2). Volunteer data from a fully sampled scan as well as data from a scan under-sampled at a true reduction factor of 6 is shown in figure 3. Ejection fraction for the fully sampled dataset was  $64.2 \pm 4.0$  % (mean  $\pm$  std. dev) and the

under-sampled data gave an ejection fraction of  $65.2 \pm 3.3 \%$ . These values were not statistically different ( $p = 0.11$ ).

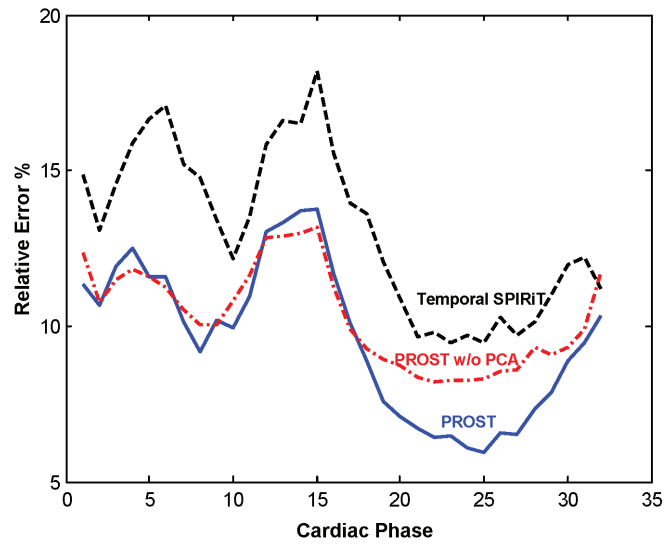


Figure 6.2: Comparison of PROST, PROST without PCA and SPIRiT in one healthy volunteer.

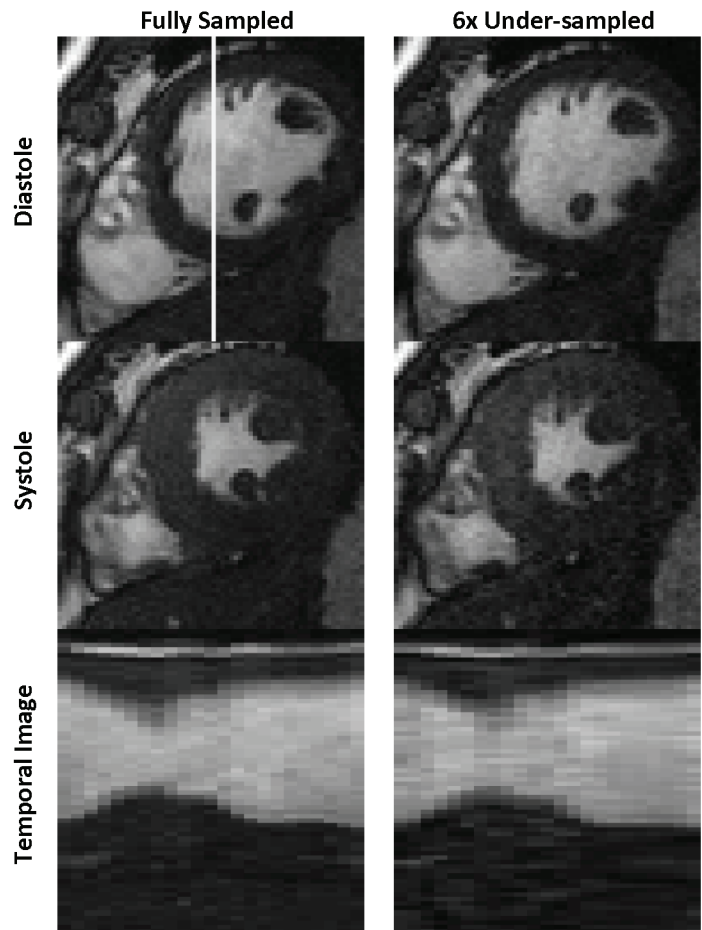


Figure 6.3: CINE images reconstructed with fully sampled and truly 6x under-sampled data in one volunteer. The time-course of an intensity profile (top left image) is shown.

## 6.5 Discussion

PROST is a SPIRiT based method that imposes temporal smoothness while allowing for arbitrary view orders. As shown in figure 6.2, PROST improves error performance compared to regular SPIRiT. During optimization, PCA improved convergence from 31 iterations (PROST w/o PCA) to 24. PCA only improved error in diastole where temporal changes are slower and easily compressible. In volunteers, reconstruction error was reduced with higher temporal resolution (8 VPS or less), due to the inherent assumptions in PROST about temporal smoothness. When used for CINE imaging, PROST gives similar ejection fraction values when compared to fully sampled data. Extensions include adding additional regularization such as L1 (4-6) and utilizing spiral/radial trajectories (3,7). PROST can be used to significantly improve temporal resolution while keeping (or reducing) the total scan time.

## 6.6 References

1. Huang F, Akao J, Vijayakumar S, Duensing GR, Limkeman M. k-t GRAPPA: a k-space implementation for dynamic MRI with high reduction factor. *Magn Reson Med* 2005;54(5):1172-1184.
2. Tsao J, Boesiger P, Pruessmann KP. k-t BLAST and k-t SENSE: dynamic MRI with high frame rate exploiting spatiotemporal correlations. *Magn Reson Med* 2003;50(5):1031-1042.
3. Seiberlich N, Lee G, Ehse P, Duerk JL, Gilkeson R, Griswold M. Improved temporal resolution in cardiac imaging using through-time spiral GRAPPA. *Magn Reson Med* 2011;66(6):1682-1688.
4. Lusting M, Santos JM, Donoho DL, Pauly JM. k-t SPARSE: High frame rate dynamic MRI exploiting spatial-temporal sparsity. 14th meeting of the International Society of Magnetic Resonance in Medicine. Seattle, Washington, USA, 2006. p. 2420.
5. Jung H, Sung K, Nayak KS, Kim EY, Ye JC. k-t FOCUSS: a general compressed sensing framework for high resolution dynamic MRI. *Magn Reson Med* 2009;61(1):103-116.

6. Lai P, Lusting M, Brau ACS, Vasanawala S. k-t SPIRiT for ultra-fast cardiac cine imaging with prospective or retrospective cardiac gating. 18th meeting of the International Society of Magnetic Resonance in Medicine. Stockholm, Sweden, 2010. p. 482.
7. Lustig M, Pauly J. SPIRiT: Iterative Self-consistent Parallel Imaging Reconstruction From Arbitrary k-Space. *Magnetic Resonance in Medicine* 2010;64(2):457-471.
8. Pedersen H, Kozerke S, Ringgaard S, Nehrke K, Kim WY. k-t PCA: temporally constrained k-t BLAST reconstruction using principal component analysis. *Magn Reson Med* 2009;62(3):706-716.
9. Liang Z. Spatiotemporal imaging with partially separable functions. 2007 4th Ieee International Symposium on Biomedical Imaging : Macro To Nano, Vols 1-3 2007:988-991.

## CHAPTER 7

### 7 HIGH SNR HIGH TEMPORAL FRAME RATE LIVER IMAGING<sup>3</sup>

#### 7.1 Abstract

High spatial-temporal four-dimensional imaging with large volume coverage is necessary to accurately capture and characterize liver lesions. Traditionally, parallel imaging and adapted sampling are used towards this goal, but they typically result in a loss of signal to noise. Furthermore, residual under-sampling artifacts can be temporally varying and complicate the quantitative analysis of contrast enhancement curves needed for pharmacokinetic modeling. We propose to overcome these problems using a novel patch-based regularization approach called Patch-based Reconstruction Of Under-sampled Data (PROUD). PROUD produces high frame rate image reconstructions by exploiting the strong similarities in spatial patches between successive time frames to overcome the severe k-space under-sampling. To validate PROUD, a numerical liver perfusion phantom was developed to characterize CNR performance compared to a previously proposed method, TRACER. A second numerical phantom was constructed to evaluate the temporal footprint and lag of PROUD and TRACER reconstructions. Finally, PROUD and TRACER were evaluated in a cohort of five liver donors. In the CNR phantom, PROUD, compared to TRACER, improved peak CNR by 3.66 times while maintaining or improving temporal fidelity. In vivo, PROUD demonstrated an average increase in CNR of 60% compared to TRACER. The results presented in this work demonstrate the feasibility

---

<sup>3</sup> Under revision: Cooper MA, Nguyen TD, Xu B, Prince MR, Elad M, Wang Y, Spincemaille P. (2014) Patch Based Reconstruction of Undersampled Data (PROUD) for High SNR and High Frame Rate Contrast Enhanced Liver Imaging. *Magn Reson Med*.

of using a combination of patch based image constraints with temporal regularization to provide high SNR, high temporal frame rate and spatial resolution four dimensional imaging.

## 7.2 Introduction

The ability to reliably capture the arterial phase in contrast enhanced imaging is crucial for the detection and characterization of liver lesions. Multiple phase imaging within a breath-hold has shown promise towards achieving this goal (1-3). To retain both high spatial and temporal resolution, parallel imaging techniques with adapted sampling schemes have been used, both with Cartesian (4-8) and radial (9-12) trajectories. The success of these techniques lies in the particular balance chosen between undersampling artifacts, signal to noise ratio (SNR), volume coverage, spatial resolution and temporal fidelity. TRACER (13), a nonlinear parallel imaging reconstruction (14) of golden ratio ordered variable density spiral acquisition, allows the reconstruction of volume covering the whole liver with a sub-second frame rate. The high temporal frame rate (equal to the time to acquire a single spiral leaf for all slice encodings) was achieved by assuming small changes of image content between frames, an assumption which is increasingly satisfied as the frame rate increases. Both in simulations and phantom experiments, a high agreement between the reconstructed and the true contrast enhancement curves was observed. However, the reconstructed images are susceptible to noise in the rapid spiral acquisition; the measured temporal footprint of each frame was found to be larger than the apparent frame rate; and

residual undersampling artifacts resulted in flickering artifacts visible when viewed in cine mode.

We propose to overcome these problems using a novel patch-based regularization approach called Patch-based Reconstruction Of Under-sampled Data (PROUD). Recently, patch-based image reconstruction methods using dictionary learning have shown promise in reconstructing both static and dynamic under-sampled MRI data (15-23) by exploiting local structure and similarity to a known dictionary. PROUD improves TRACER image quality by exploiting similarities in spatial patches (24-26) between temporal frames that are relatively close ( $\sim 250$ ms). Through phantom and in vivo studies, it is shown that PROUD is able to maintain the high spatial and temporal frame rate obtained with TRACER while allowing for increased SNR, reduction of temporal footprint, and reduced undersampling artifacts.

### 7.3 Theory

The regularization used in PROUD is based on the observation that the local structure of the image is largely preserved between successive frame rates in high frame rate dynamic imaging. In previous approaches (13,14), differences between successive frames were constrained on a global, image based level. To constrain differences on a local level, we use image patches. Patch based image regularization has proven very successful in image processing algorithms such as denoising (24).

In this work, each  $n \times n$  patch  $R_{i,j}v$  around pixel  $(i, j)$  of the unknown image  $v$  is assumed to be a linear combination of a small number of  $n \times n$  patches taken from a dictionary of patches  $P_{i,j}D$  specific to the pixel  $(i, j)$ . This dictionary is constructed by taking  $n \times n$  patches from an  $m \times m$  neighborhood around the pixel  $(i, j)$  selected by  $P_{i,j}$  from a set  $D$  of a known reference images that are assumed to represent the local structure of the unknown image  $v$  well. Therefore, the following minimization problem was solved in order to obtain a solution  $v_t^*$  for each time  $t = 1, \dots, T$ :

$$v_t^* = \operatorname{argmin}_{v_t, \alpha_{i,j,t}} \|U_t F S v_t - y_t\|_2^2 + \lambda \sum_{i,j} \|R_{i,j} v_t - \alpha_{i,j,t} P_{i,j} D_t\|_2^2 \quad \text{such that } \|\alpha_{i,j,t}\|_0 = 1 \quad [7.1]$$

where  $y_t$  is the sampled k-space data for all coils,  $T$  is the total number of time frames,  $S$  is the operator that multiplies the image  $v_t$  with each of the coil sensitivities  $(s_i)_{i=1, \dots, N_c}$ ,  $N_c$  is the number of coils,  $F$  is the spatial Fourier transform,  $U_t$  is the projection of k-space unto the spiral leaf acquired at time  $t$ . The  $L_0$  norm constraint on the vector  $\alpha_{i,j,t}$  ensures that only one basis of patches from the dictionary  $P_{i,j}D_t$  is selected. This reflects the constraint that an image patch is expected to move only slightly between time frames and can change in scale as well. The latter will be the case for contrast enhanced imaging. A general depiction of Eq. [7.1] for one time frame is shown in Fig. 7.1.

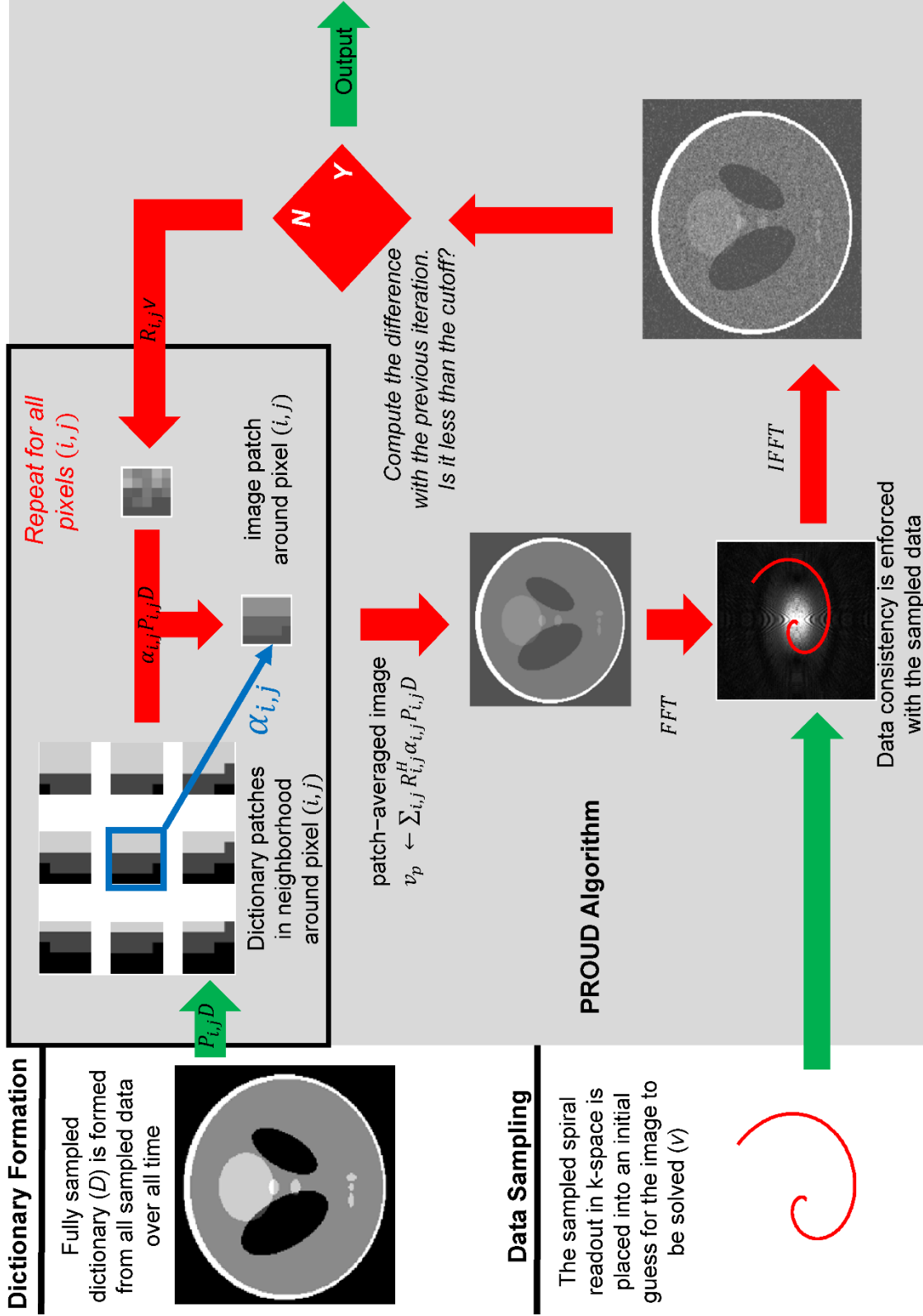


Figure 7.1: A diagram of the PROUD reconstruction algorithm for one temporal frame. Patch size is 5x5 with a neighborhood size of 7x7.

$D_t$  was constructed from multiple reference images: the previously reconstructed image  $v_{t-1}^*$  and a composite image reconstructed from all acquired data, which in dynamic imaging is fully sampled or even oversampled. In vivo, to further improve robustness to through plane motion,  $D_t$  included images derived from  $N_{slices}$  neighboring slices reconstructed from all acquired data as well. As in TRACER (13), an initial guess  $v_0$  for the first frame was reconstructed from the first fully sampled set of data. The coil sensitivities  $(s_i)_{i=1,\dots,N_c}$  are derived by dividing low resolution coil images by their root sum of squares. These low resolution coil images were obtained from all acquired data in the dynamic acquisition, which typically is long enough to provide a highly oversampled, high SNR reconstruction. The determination of the regularization parameter  $\lambda$  is described below.

For high temporal resolution imaging, a new frame is reconstructed for each newly acquired set of k-space data (13), which is assumed to be acquired in a small time interval in order to satisfy the assumption of smooth temporal changes. With PROUD (and TRACER), a single spiral leaf (collected for all slice encodings in the case of 3D imaging) is used to update each temporal frame, typically at a rate of  $\sim 250$  ms. The angle between two successive spiral leaves is based on the golden ratio (13,27,28).

In a second step, temporal smoothness was enforced to overcome the temporally varying residual undersampling artifacts in the reconstructed images. This

regularization provides smooth time courses for contrast enhancement curves simplifying post-processing. This was done by solving:

$$v_{t=1,\dots,T}^* = \underset{v_t, \alpha_{i,j,t}}{\operatorname{argmin}} \left\{ \sum_{t=1}^T \|U_t F S v_t - y_t\|_2^2 + \lambda \sum_{t=1}^T \sum_{i,j} \|R_{i,j} v_t - \alpha_{i,j,t} P_{i,j} D_t\|_2^2 + \gamma \sum_{t=1}^T \|v_t - (v_{t-1} + v_{t+1})/2\|_2^2 \right\} \quad [7.2]$$

such that  $\|\alpha_{i,j,t}\|_0 = 1$  for all  $t = 1, \dots, T$ ,

Eqs. [7.1] and [7.2] are solved by extending the method used in (25) to the multi-channel non-Cartesian case. A detailed derivation is shown in Appendix B. The solver algorithm iterates between solving for  $\alpha_{i,j,t}$  and solving for  $v_t$ . Since spiral data was acquired in this study, non-uniform fast Fourier transforms were performed using NUFFT (29,30). The dictionary  $D_t$  for each frame  $v_t$  was constructed in the same way as for Eq [7.1].

The patch and temporal regularization parameters,  $\lambda$  and  $\gamma$ , were determined automatically by the solver. To find  $\lambda$ , we estimated a solution for  $v_1^*$  by excluding the regularization term from Eq [7.1]:

$$v_1^* = \underset{v_1}{\operatorname{argmin}} \|U_1 F S v_1 - y_1\|_2^2 \quad [7.3]$$

Because of the severe undersampling by  $U_1$ , which projects onto a single leaf, this was iteratively solved by using  $v_0$  as the initial guess and halting the iterations when the image update between iterations no longer decreased, similar to the stopping criterium used in TRACER (13). Next, a vector  $\alpha_{i,j,1}^*$  was found by solving (see Appendix B):

$$\alpha_{i,j,1}^* = \underset{\alpha_{i,j,1}}{\operatorname{argmin}} \sum_{i,j} \|R_{i,j}v_1^* - \alpha_{i,j,1}P_{i,j}D_t\|_2^2 \text{ such that } \|\alpha_{i,j,1}\|_0 = 1 \quad [7.4]$$

Using the discrepancy principle (31), the regularization parameter  $\lambda$  was then chosen such that the two terms in Eq. [7.1] were equal for the values of  $v_1^*$  and  $\alpha_{i,j,1}^*$  obtained in Eqs. 7.3 and 7.4, respectively. The value of  $\lambda$  was then kept constant for all remaining time frames. After Eq. [7.1] was solved for all time frames, the regularization parameter  $\gamma$  was obtained by demanding that the first term (data term) equaled the third term (temporal term) in Eq. [7.2] when  $v_t^*$  and  $\alpha_{i,j,t}^*$  ( $t = 1, \dots, T$ ) were set to the solutions of Eq. [7.1].

Appendix A outlines the PROUD reconstruction algorithm in detail.

## 7.4 Methods

### *7.4.1 Optimization of reconstruction parameters*

To characterize the PROUD algorithm, a numerical phantom simulating dynamic liver perfusion was created (Fig. 7.2a) similar to the phantom in (13). The noiseless phantom  $v_t^{REF}$  ( $t = 1, \dots, T$ ) was multiplied by simulated coil sensitivity maps, and sampled with a spiral trajectory. For each time frame, a cutoff of  $r_{cutoff} = 10^{-5}$  with a maximum of 100 iterations was used. Five temporal iterations were used in solving Eq. [7.2]. The patch size was determined by solving Eq. [7.1] for a range of sizes: square patches of size  $n = 3, 6, 7, 9, 11$  and 13 pixels were tested. The root mean square error  $RMSE$ , defined as:

$$RMSE = \sqrt{\sum_t \|v_t - v_t^{REF}\|_2^2} \quad [7.5]$$

was calculated to determine the optimal patch size. The background of the phantom was excluded from the norm in Eq. [7.5]. The neighborhood size was then set  $m = n + 2$  to reduce the increase in computation time while still allowing small local translational motions of image patches between successive time frames.

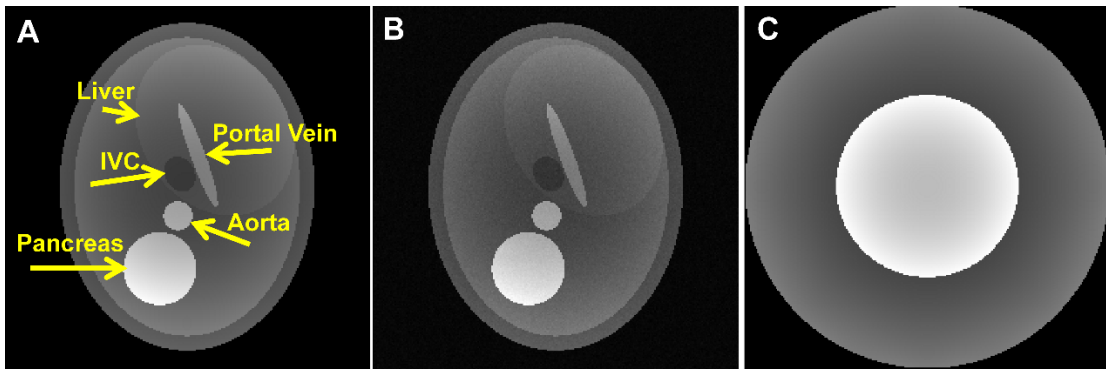


Figure 7.2: A) A numerical phantom simulating liver perfusion. B) The phantom in A, with noise added. C) Temporal footprint phantom with inner diameter =  $0.25 \cdot FOV$ .

#### 7.4.2 Numerical phantom SNR

Thirty sets of randomly generated Gaussian noise was added to the numerical phantom described above (Fig. 7.2b). A fully sampled first frame was assumed. The phantoms were then reconstructed using PROUD with the reconstruction parameters obtained above and using the TRACER algorithm (13) for comparison. A contrast-to-noise ratio  $CNR$  was computed as:

$$CNR = SNR_{aorta} - SNR_{portal\ vein} \quad [7.6]$$

where  $SNR_{aorta}$  and  $SNR_{portal\ vein}$  are the signal-to-noise ratios within a region of interest (ROI) in the respective anatomies. Pixel-wise  $SNR$  was computed at each time-point by taking the mean of each pixel in an ROI over the 30 reconstructions divided by the standard deviation of each pixel. The mean of the pixel-wise  $SNR$  values was then taken over the ROI.

#### 7.4.3 Numerical phantom temporal footprint

Temporal phantoms were developed (Fig. 7.2c) to characterize the temporal response of the PROUD algorithm compared to TRACER. Each phantom consists of a central disk with diameter (DIA) equal to 0.125, 0.1875, 0.25, 0.3125, 0.375, 0.4375, 0.5, 0.5625, 0.625, 0.6875, 0.75, 0.8125, 0.875, 0.9375, 1 times the FOV superimposed onto a larger disk with diameter equal to the FOV. The contrast in the central disk was changing over time, such that the enhancement curve was Gaussian. The temporal footprint (TF), used to characterize the length of the enhancement curves, was defined as the full width-half maximum (FWHM) of the Gaussian curves:  $WHM = 2\sqrt{2\ln 2}\sigma$ . The TF of the curves was varied between 0.5, 1, 2, 5, 7, 10, 15 and 20 seconds. This resulted in 120 unique numerical phantoms. These noiseless phantoms were multiplied by simulated coil sensitivity maps and sampled along a spiral trajectory. A fully sampled first frame was assumed and the phantom was reconstructed with PROUD and TRACER for comparison. For PROUD, the phantoms were reconstructed both with Eq. 1 and 2 to allow for analysis of the effects of temporal regularization. The

phantoms allowed for the estimation of the temporal footprint and lag. The reconstructed curve was temporally shifted and compressed to maximize its cross-correlation with respect to the true simulated curve. The measured temporal footprint ( $TF_{MEAS}$ ) of the reconstructed curve was taken as the true temporal footprint divided by the obtained compression factor. The measured temporal lag was defined as the obtained temporal shift (in sec). Differences in the amplitude of the measured curve compared to the true curve were not taken into account.

#### 7.4.4 *In vivo liver MRI experiments*

In vivo data were acquired using a golden angle 3D dynamic multi-phase spiral LAVA sequence using a stack of variable density spiral trajectory (1,13). Five candidate liver donors imaged with this acquisition were selected retrospectively in accordance with an institutionally approved IRB protocol. The acquisition acquired data continuously for 60 sec, while the patients were given repeated breath-hold instructions. Since breathing motion was present, additional high SNR images created from all sampled data at 3 slices above and below the reconstructed slice were added to the dictionary  $D_t$ .

CNR was computed in vivo as:

$$CNR = (S_{aorta} - S_{portal\ vein})/N_{liver} \quad [7.7]$$

where  $S_{aorta}$  and  $S_{portal\ vein}$  is the mean signal in a ROI in the aorta and portal vein, respectively, and  $N_{liver}$  the signal standard deviation in an ROI of homogenous liver tissue near both the aorta and portal vein ROIs. This is computed for each time frame and is a surrogate measure for how well the arterial phase is visualized (13).

All PROUD and TRACER reconstructions were done either on a Dell Studio XPS 8100 (Intel i7 2.8 GHz processor, 16 GB RAM, Windows 7, Matlab R2011b) or a Dell PowerEdge R910 Server (64 cores, 64 GB RAM, Red Hat Linux, Matlab R2009a). Statistical significance ( $p < 0.05$ ) was determined by using a paired two-tailed student's t-test in Microsoft Excel 2013.

## 7.5 Results

### *7.5.1 Parameter selection*

Optimal patch size was determined to be 7x7 pixels as it resulted in the smallest RMSE (Figure 6.3) and neighborhood size was then set to be 9x9 pixels.

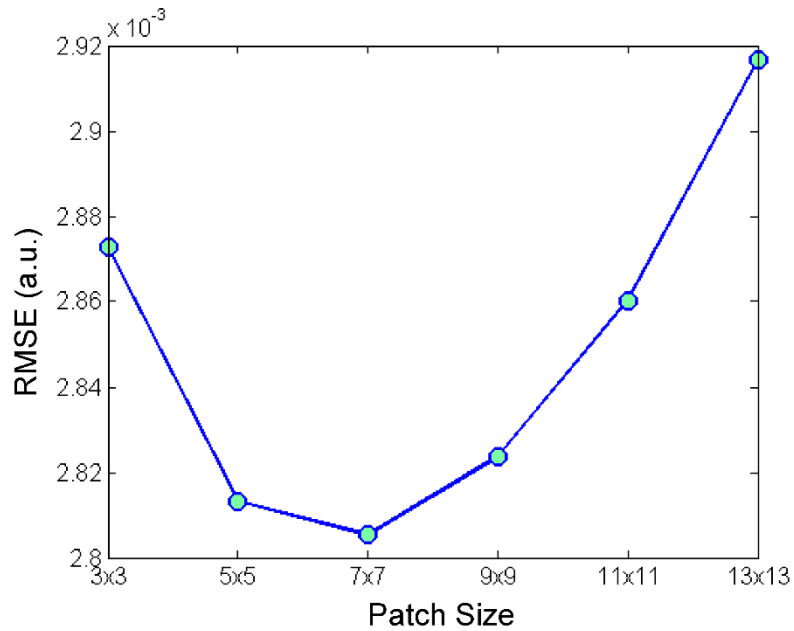


*Figure 7.3: Root Mean Squared Error (RMSE) vs. patch size. 7x7 pixels was chosen to be the optimal patch size.*

### 7.5.2 Phantom SNR test

Both algorithms provided similar contrast enhancement curves (Fig 7.4A). However, PROUD provided almost 3.66x higher peak *CNR* compared to TRACER (Fig. 7.4B). The dip in the PROUD *CNR* was due to increased undersampling artifacts associated with rapid signal changes, such as the enhancing aorta and portal vein.

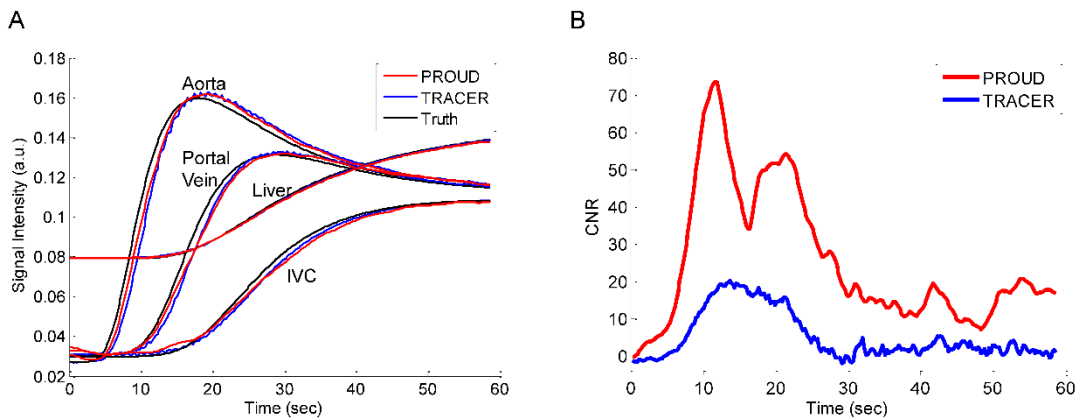


Figure 7.4: A) Average signal intensity of various regions of interest in the numerical phantom with noise standard deviation = 0.003. B) CNR averaged over 30 noisy phantoms of PROUD compared to TRACER. The dip in CNR of the PROUD curve is due increased reconstruction errors at the edges of the aorta and portal vein, which increase the standard deviation in the ROIS near the edges.

### 7.5.3 Phantom temporal footprint

Fig. 7.5 shows the results from the testing of the temporal response of PROUD compared to TRACER. For larger objects (>50% FOV) and longer temporal footprint (> 5 sec), the curves reconstructed with TRACER and PROUD had measured temporal footprints that were very close to those of the reference curves and temporal lags below 0.5 seconds.

For all methods, temporal lag decreased for larger objects and increased for larger temporal footprint. Overall TRACER had a higher temporal lag than PROUD. In addition, there was a larger discrepancy between TRACER and PROUD for smaller objects (FOV 12.5%-43.8%). For larger objects (FOV = 81.3% and greater) with very short temporal events (0.5 - 1 sec temporal footprint), PROUD had a longer temporal lag than TRACER.

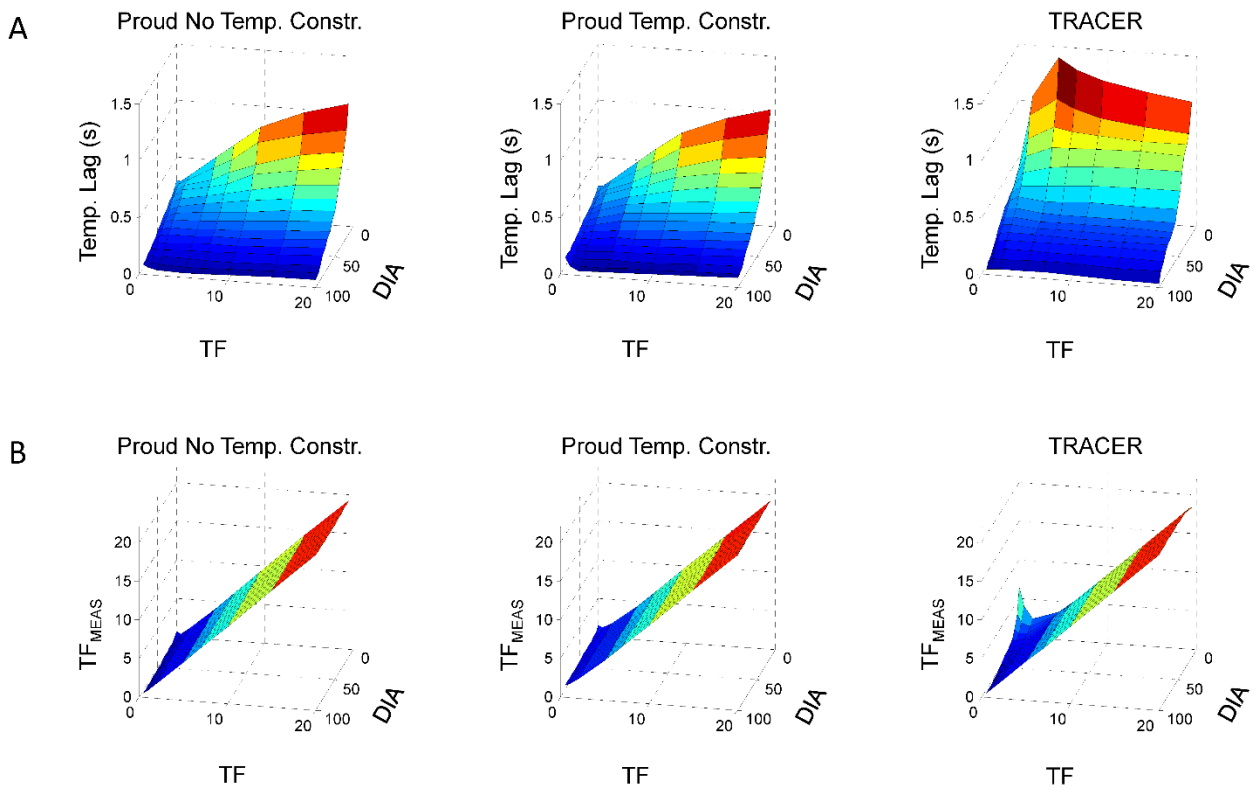


Figure 7.5: A) Temporal (Temp.) lag and B) measured temporal footprint ( $TF_{MEAS}$ ) values determined using cross-correlations of the reconstructions from TRACER and PROUD compared to the true phantom curves with varying diameter (DIA) and temporal footprint (TF). PROUD No. Temp. Constr. is after solving Eq. [7.1] and PROUD Temp. Constr. is after solving Eq. [7.2].

The measured temporal footprint for TRACER and PROUD were similar for objects of size 37.5% of the FOV and greater. The PROUD reconstruction using temporal regularization (Eq. [7.2]) had a slightly larger measured temporal footprint compared to the PROUD reconstruction without (Eq. [7.1]). In addition, for fast temporal events ( $\sim 5$  sec temporal footprint and less), there was some discrepancy in the methods. In general, for smaller objects TRACER had an increased measured temporal footprint. However, from objects sized equal or greater than 50% of the FOV, the temporal regularization of Eq. [7.2] made the measured temporal footprint larger than both TRACER and PROUD without the temporal regularization, with the largest difference around 1 sec. Finally for the three smallest objects (FOV = 12.5 – 25%), the measured TRACER temporal footprint is smaller than the true temporal footprint, when the latter exceeds 2 to 3 sec.

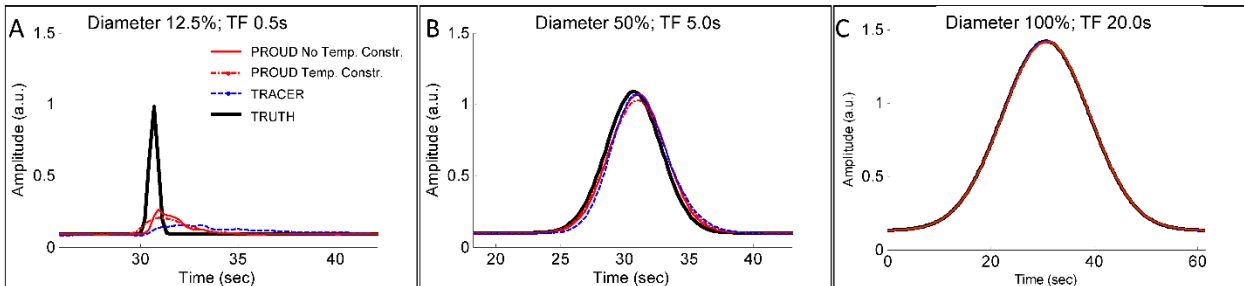


Figure 7.6: Examples of curves analyzed in Fig.7. 5. A) A very short temporal event (TF = 0.5 sec) with a small diameter object (12.5% FOV). B) A medium size temporal event (TF = 5 sec) with a mid-sized diameter object (50% FOV). C) A long temporal event (TF = 20 sec) with a large diameter object (100% FOV).

Fig. 7.6 shows examples for three of the curves analyzed in Fig. 7.5. In Fig. 7.6A for a short TF with small DIA, TRACER (TFMEAS =7.5s , Temp. Lag =1.9s ), PROUD No Temp. Constr. (TFMEAS = 1.6s, Temp. Lag =1.6s) and PROUD w/ Temp. Constr. (TFMEAS =2.4s , Temp. Lag =1.4s) had large errors in reconstructing the true curve. In Fig. 7.6B as the TF and DIA grow, TRACER (TFMEAS =5.1s , Temp. Lag =1.8s), PROUD No Temp. Constr. (TFMEAS = 5.1s, Temp. Lag =1.4s) and PROUD w/ Temp. Constr. (TFMEAS = 5.3s, Temp. Lag =1.3s), had improved performance compared to the smaller DIA/TF. Finally in Fig. 7.6C with a large TF and DIA, all methods provided curves similar to the truth: TRACER (TFMEAS = 20.0, Temp. Lag =0.1s), PROUD No Temp. Constr. (TFMEAS = 20.0s, Temp. Lag =0.3s) and PROUD w/ Temp. Constr. (TFMEAS =20.1s , Temp. Lag =0.3s).

#### 7.5.4 *In vivo testing*

Over the 5 in vivo datasets, the images reconstructed using PROUD had a peak *CNR* of  $42 \pm 18$  compared to  $26 \pm 12$  using TRACER resulting in a 60% improvement in peak *CNR* ( $p = 0.008$ ). Fig. 7.7 shows a temporal frame reconstructed with the PROUD and TRACER methods. TRACER clearly suffers from increased noise in the reconstruction. Fig. 7.8 shows the enhanced and *CNR* curves for patient in Fig. 7.7. In-vivo for Eq. [7.1], the preliminary pure Matlab (Natick , MA) implementation of PROUD took an average of  $4.3 \pm 0.1$  minutes to reconstruct one temporal frame (as

measured in one volunteer).

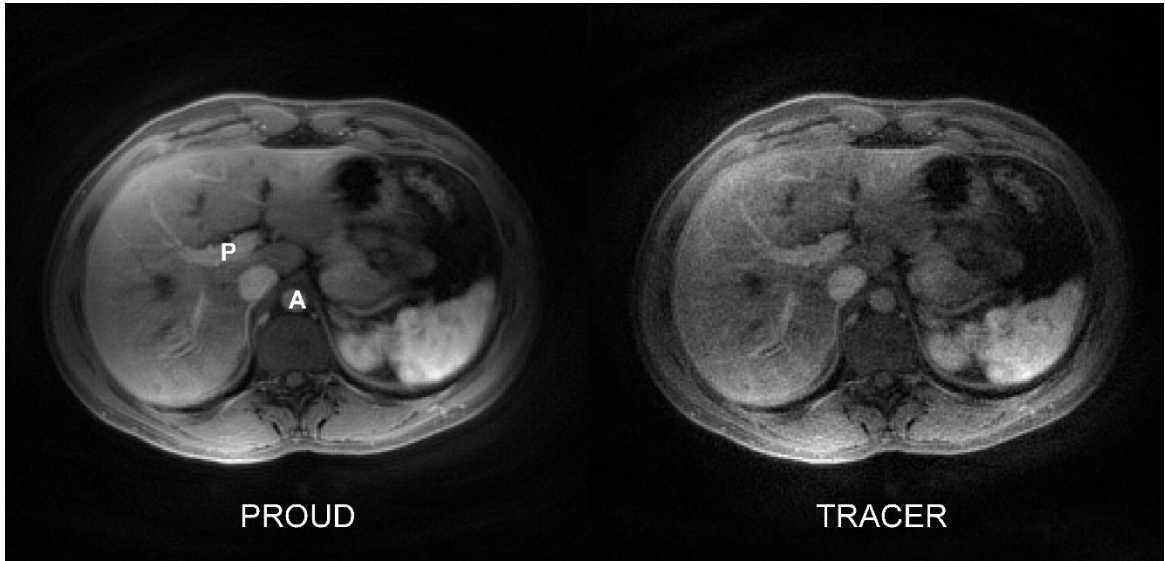


Figure 7.7: In vivo image reconstruction using PROUD (left) and TRACER (right). Notice the reduction in noise (increase in SNR) utilizing the PROUD method.

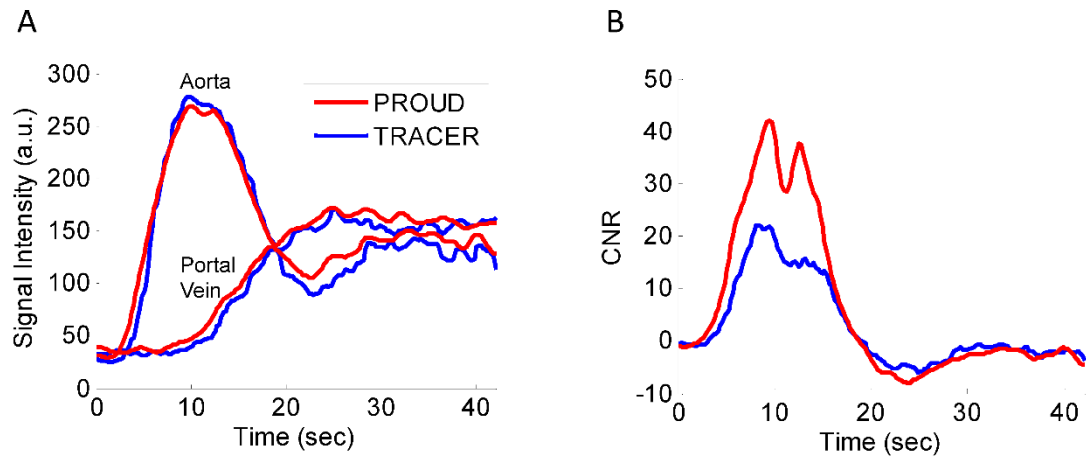


Figure 7.8: A) In vivo perfusion curves and B) CNR curves for the same volunteer as in Fig. 7.7.

## 7.6 Discussion

The results presented in this work demonstrate the feasibility of using a combination of a patch based image constraint with a temporal regularization to provide improved CNR in phantoms while maintaining or improving temporal fidelity and to provide an increase in CNR of up to 60% in vivo compared to TRACER. This reduction in noise (as seen by the increase in CNR) can be attributed to the patch-based dictionary methods employed in the PROUD method. Patch level dictionary learning has previously been shown to be useful in de-noising problems (24,26) and has been shown to improve PSNR compared to a ground truth in MRI data (25).

Temporal characterization of PROUD against TRACER gave similar performance for larger objects and slower temporal events. For short temporal events or small objects there were some discrepancies between the methods. TRACER had increased temporal lag and somewhat larger measured temporal footprint with smaller object size at shorter temporal events. This may be due to differences in the reconstruction methods of TRACER and PROUD. Importantly, TRACER is subject to blurring of edges during fast signal changes. This is shown in Fig. 4d of (13). This blurring will effect smaller objects more and is most likely the cause of the increase in the measured temporal footprint and some of the temporal lag. This artifact was reduced in PROUD, however, since the dictionary-based method allows for a better delineation of edges during contrast changes. This is because this edge information is available in the image reconstructed from all available data which was used in the dictionary for each

frame. In addition, with PROUD regularization is done on a local level while TRACER implements global image regularization. In our analysis, the method of determining the temporal lag and compression factor via compression and cross-correlation may be affected by the fact that response function in TRACER only is non-zero for positive time, see Fig. 3a in (13), while, due the temporal smoothness constraint, PROUD has a bi-directional temporal spread. These reasons may also explain the reason why TRACER exhibits an apparent negative lag for the three smallest objects (FOV = 12.5 – 25%), which is likely an artifact of the specific way in which lag was measured in this work. Overall it is important to note, that for both methods, temporal response was a factor of both the temporal event length and the size of the feature being evaluated.

Finally, in comparison to TRACER, PROUD is able to reduce residual temporal flickering artifacts due to the addition of Eq. 7.2. This temporal fidelity constraint forces neighboring frames to be similar over time therefore penalizing rapid temporal changes (e.g. flickering). There are differences to be noted however in the temporal performance of PROUD with Eq. 7.1 only and PROUD with Eq. 7.2. In general, Eq. 7.1 (and sometimes TRACER with larger objects) provided slightly better measured temporal footprint than Eq. 7.2. This is mainly due to the fact that the temporal term in Eq. 7.2. may introduce some degree of temporal blurring. The effect of temporal blurring was observed to be small, except in fast changing temporal signals.

Improvement may be possible in future implementations replacing the  $L_2$ -norm on the temporal term with an  $L_1$  norm.

There were some limitations in this work. In vivo validation was only done in subjects that were assumed to be healthy. Further studies may be warranted to evaluate the performance of PROUD in patients presenting with liver dysfunction (i.e. fibrosis, hepatocellular carcinoma, etc.). In addition, reconstruction time for the current pure Matlab implementation of PROUD was long (4.3 minutes to reconstruct one frame of one slice with Eq. [7.1]). However, reconstruction time can be reduced through implementation in C code and GPU parallelization. Future implementations of PROUD may warrant automatic patch and neighborhood size determination, which could be done by analyzing the residual in Eq. [7.10a] for varying patch/neighborhood size. If patch size were to be determined automatically, it could lead to an overall reduction in reconstruction time, since it would make the search for  $\alpha_{i,j}$  less computationally expensive.

### 7.7 Conclusion

The proposed PROUD algorithm combines an image patch based regularization combined with a temporal constraint to enable high SNR, high temporal frame rate and spatial resolution 4D imaging that can improve in vivo peak  $CNR$  by up to 60% compared to previous methods while maintaining adequate temporal fidelity.

## 7.8 Appendix A

$v_t, \alpha_{i,j,t} \leftarrow PROUD(y_t)$

- 1) Reconstruct a reference  $v_0$  using the first  $N_S$  spiral leaves
- 2) Reconstruct a composite image  $v_{ALL}$  using all spiral leaves
- 3) Compute the coil sensitivity maps  $(s_i)_{i=1,\dots,N_c}$  using  $v_{ALL}$
- 4) Solve Eqs [7.3] and [7.4], obtaining initial estimates of  $v_1^*$  and  $\alpha_{i,j,1}^*$
- 5) Set  $\lambda$  such that the two terms in Eq [7.1] are equal for the solutions in step 4.
- 6) Solve Eq [7.1] for all time frames:

**for**  $t = 1, \dots, T$

$$v_t^0 \leftarrow v_{t-1} + S^H F^H U_t^H (y_t - U_t F S v_{t-1})$$

$$v_{prev} \leftarrow v_t^0 \text{ and } k \leftarrow 0$$

$$r \leftarrow \|v_t^0 - v_{prev}\| / \|v_t^0\|$$

$$D_t \leftarrow DICTIONARY(v_{t-1}, v_{ALL})$$

**while**  $r \geq r_{cutoff}$

find  $\alpha_{i,j,t}^k$  by fitting  $v_t^k$  against patch dictionary  $D_t$  using Eq. [7.10a,b]

$$\text{create the patch averaged image } v_p^k \leftarrow \sum_{i,j} R_{i,j}^H \alpha_{i,j,t}^k P_{i,j} D_t$$

compute new image estimate  $v_t^k$  using Eq. [7.9a]

$$r \leftarrow \|v_t^k - v_{prev}\| / \|v_t^k\|$$

$$v_{prev} \leftarrow v_t^k \text{ and } k \leftarrow k + 1$$

**end**

$$v_t \leftarrow v_t^k \text{ and } \alpha_{i,j,t} \leftarrow \alpha_{i,j,t}^k$$

**end**

- 7) Set  $\gamma$  such that the terms 1 and 3 in Eq [7.2] are equal for the solutions obtained in step 5.

- 8) Solve Eq. [7.2] using the solutions obtained in step 5 as initial guess:

$$v_{t,1} \leftarrow v_t \text{ and } \alpha_{i,j,t,1} \leftarrow \alpha_{i,j,t}$$

**for**  $m = 2, \dots, N_{iter}^t$

**for**  $t = 1, \dots, T$

$$v_{t,m} \leftarrow v_{t-1,m} + S^H F^H U_t^H (y_t - U_t F S v_{t-1,m})$$

$$v_a \leftarrow 1/2 (v_{t-1,m} + v_{t+1,m-1}).$$

$$D_{t,m} \leftarrow DICTIONARY(v_{t-1,m}, v_{ALL})$$

find  $\alpha_{i,j,t,m}$  by fitting  $v_{t,m}$  against patch dictionary  $D_{t,m}$  using Eq. [7.10a,b]

$$\text{create the patch averaged image } v_{p,m} \leftarrow \sum_{i,j} R_{i,j}^H \alpha_{i,j,t,m} P_{i,j} D_{t,m}$$

compute new image estimate  $v_{t,m}$  using Eq. [7.9b]

**end**

**end**

$$v_t \leftarrow v_{t,m} \text{ and } \alpha_{i,j,t} \leftarrow \alpha_{i,j,t,m}$$

$$D \leftarrow DICTIONARY(v_1, \dots, v_{N_d})$$

- 1) For every pixel  $(i, j)$  construct a set  $d_{i,j}$  of  $N_d$  patches of size  $n \times n$  centered on pixel  $i, j$ .
- 2) Orthonormalize each set  $d_{i,j}$
- 3) For every pixel  $(i, j)$  collect all sets  $d_{a,b}$  in a  $m \times m$  neighborhood centered on pixel  $i, j$

## 7.9 Appendix B

In the following, we detail the solver used for Eq. [7.1] and [7.2]. The method goes back and forward between solving for  $v_t^*$  and solving for the patch weights  $\alpha_{i,j,t}$ .

Eqs. [7.1] and [7.2] are solved by extending the method in (25) to the multi-channel non-Cartesian case. We start by assuming  $\alpha_{i,j,t}$  to be fixed to some appropriate initial values. Then Eq. [7.11]

$$v_t^* = \underset{v_t}{\operatorname{argmin}} \|U_t F S v_t - y_t\|_2^2 + \lambda \sum_{i,j} \|R_{i,j} v_t - \alpha_{i,j,t} P_{i,j} D_t\|_2^2$$

A solution for  $v_t^*$  is obtained by setting the derivative of the cost function to zero, resulting in

$$[S^H F^H U_t^H U_t F S + \lambda \sum_{i,j} R_{i,j}^H R_{i,j}] v_t^* = S^H F^H U_t^H y_t + \lambda \sum_{i,j} R_{i,j}^H \alpha_{i,j,t} P_{i,j} D_t$$

Where  $R_{i,j}^H R_{i,j}$  is equal to  $\beta I$  where  $\beta$  is a scaling factor equal to  $n^2$ , after appropriately taking into account patches at the edge of the FOV. Therefore:

$$[S^H F^H U_t^H U_t F S + \lambda \beta I] v_t^* = S^H F^H U_t^H y_t + \lambda \sum_{i,j} R_{i,j}^H \alpha_{i,j,t} P_{i,j} D_t$$

Note that  $S^H F^H F S = S^H S = I$ , by the fact that the Fourier transform is unitary and the fact that  $S^H S$  is a diagonal matrix with entries equal to  $\sum_i |s_i^2| = 1$  (by construction). Therefore

$$S^H F^H (U_t^H U_t + \lambda \beta I) F S v_t^* = S^H F^H U_t^H y_t + \lambda \sum_{i,j} R_{i,j}^H \alpha_{i,j,t} P_{i,j} D_t$$

By applying  $FS$  on both sides, we obtain

$$(U_t^H U_t + \lambda \beta I) FS v_t^* = U_t^H y_t + FS \lambda \beta v_p \quad [7.8]$$

where  $v_p = \frac{1}{\beta} \sum_{i,j} R_{i,j}^H \alpha_{i,j,t} P_{i,j} D_t$  is the ‘‘patch averaged image’’. Here  $U_t^H U_t$  ‘‘zeroes out’’ any k-space that is not on the spiral trajectory corresponding to time frame  $t$ . By writing  $FS \lambda \beta v_p = U_t^H U_t FS \lambda \beta v_p + (1 - U_t^H U_t) FS \lambda \beta v_p$ , we can apply the inverse of the diagonal matrix on both sides of Eq. [7.8]:

$$FS v_t^* = \frac{1}{1 + \lambda \beta} (U_t^H y_t + U_t^H U_t FS \lambda \beta v_p) + \frac{1}{\lambda \beta} (1 - U_t^H U_t) FS \lambda \beta v_p$$

$U_t^H y_t$  is simply the sampled k-space locations zero-padded to the matrix size.  $\beta$  can be incorporated into  $\lambda$  such that we can substitute  $\lambda \leftarrow \beta \lambda$  as in (25). This can be simplified to

$$v_t^* = v_p + \frac{1}{1 + \lambda} S^H F^H U_t^H (y_t - U_t FS v_p) \quad [7.9a]$$

The added temporal regularization term in Eq. [2] similarly leads to:

$$v_t^* = \frac{\lambda v_p + \gamma v_a}{\lambda + \gamma} + \frac{1}{1 + \lambda + \gamma} S^H F^H U_t^H \left( y_t - U_t FS \frac{\lambda v_p + \gamma v_a}{\lambda + \gamma} \right) \quad [7.9b]$$

Where  $v_a = \frac{1}{2} (v_{t-1}^* + v_{t+1}^*)$ . To speed up convergence, new estimates of  $v_t^*$  are used in the initialization and in the regularization term for subsequent time frames as soon as they become available.

Once an updated guess for an image  $v$  is available, the patch weights  $\alpha_{i,j,t}$  are updated as follows. For every pixel  $(i, j)$ , the following optimization is performed

$$d^* = \operatorname{argmax}_{d \in P_{i,j}D} |A(d, R_{i,j}v)| \quad [7.10a]$$

Where  $A(d, R_{i,j}v) \stackrel{\text{def}}{=}} \sum_{w \in d} w^H R_{i,j}v$  is the projection of patch  $R_{i,j}v$  onto the basis  $d$  of patches from the dictionary, which, by construction, is an orthonormal basis. Once the optimal patch set  $d^*$  is found, the patch weights are set equal to the linear coefficients in this basis:

$$\alpha_{i,j} = \{w^H R_{i,j}v\}_{w \in d^*} \quad [7.10b]$$

## 7.10 References

1. Agrawal MD, Spincemaille P, Mennitt KW, Xu B, Wang Y, Dutruel SP, Prince MR. Improved hepatic arterial phase MRI with 3-second temporal resolution. *J Magn Reson Imaging* 2013;37(5):1129-1136.
2. Ito K, Fujita T, Shimizu A, Koike S, Sasaki K, Matsunaga N, Hibino S, Yuhara M. Multiarterial phase dynamic MRI of small early enhancing hepatic lesions in cirrhosis or chronic hepatitis: differentiating between hypervascular hepatocellular carcinomas and pseudolesions. *AJR Am J Roentgenol* 2004;183(3):699-705.
3. Hong HS, Kim HS, Kim MJ, De Becker J, Mitchell DG, Kanematsu M. Single breath-hold multiarterial dynamic MRI of the liver at 3T using a 3D fat-suppressed keyhole technique. *J Magn Reson Imaging* 2008;28(2):396-402.
4. Saranathan M, Rettmann DW, Hargreaves BA, Clarke SE, Vasawala SS. Differential Subsampling with Cartesian Ordering (DISCO): a high spatio-temporal resolution Dixon imaging sequence for multiphasic contrast enhanced abdominal imaging. *J Magn Reson Imaging* 2012;35(6):1484-1492.
5. Low RN, Bayram E, Panchal NJ, Estkowski L. High-resolution double arterial phase hepatic MRI using adaptive 2D centric view ordering: initial clinical experience. *AJR Am J Roentgenol* 2010;194(4):947-956.

6. Saranathan M, Rettmann D, Bayram E, Lee C, Glockner J. Multiecho time-resolved acquisition (META): a high spatiotemporal resolution Dixon imaging sequence for dynamic contrast-enhanced MRI. *J Magn Reson Imaging* 2009;29(6):1406-1413.
7. Wang K, Schiebler ML, Francois CJ, Del Rio AM, Cornejo MD, Bell LC, Korosec FR, Brittain JH, Holmes JH, Nagle SK. Pulmonary perfusion MRI using interleaved variable density sampling and HighLY constrained cartesian reconstruction (HYCR). *J Magn Reson Imaging* 2013;38(3):751-756.
8. Feng L, Srichai MB, Lim RP, Harrison A, King W, Adluru G, Dibella EV, Sodickson DK, Otazo R, Kim D. Highly accelerated real-time cardiac cine MRI using k-t SPARSE-SENSE. *Magn Reson Med* 2013;70(1):64-74.
9. Brodsky EK, Bultman EM, Johnson KM, Horng DE, Schelman WR, Block WF, Reeder SB. High-spatial and high-temporal resolution dynamic contrast-enhanced perfusion imaging of the liver with time-resolved three-dimensional radial MRI. *Magn Reson Med* 2013;71(3):934-941.
10. Feng L, Grimm R, Block KT, Chandarana H, Kim S, Xu J, Axel L, Sodickson DK, Otazo R. Golden-angle radial sparse parallel MRI: Combination of compressed sensing, parallel imaging, and golden-angle radial sampling for fast and flexible dynamic volumetric MRI. *Magn Reson Med* 2013;10.1002/mrm.24980.

11. Seiberlich N, Ehse P, Duerk J, Gilkeson R, Griswold M. Improved radial GRAPPA calibration for real-time free-breathing cardiac imaging. *Magn Reson Med* 2011;65(2):492-505.
12. Wright KL, Lee GR, Ehse P, Griswold MA, Gulani V, Seiberlich N. Three-dimensional through-time radial GRAPPA for renal MR angiography. *J Magn Reson Imaging* 2014;10.1002/jmri.24439.
13. Xu B, Spincemille P, Chen G, Agrawal M, Nguyen TD, Prince MR, Wang Y. Fast 3D contrast enhanced MRI of the liver using temporal resolution acceleration with constrained evolution reconstruction. *Magn Reson Med* 2013;69(2):370-381.
14. Uecker M, Zhang S, Frahm J. Nonlinear inverse reconstruction for real-time MRI of the human heart using undersampled radial FLASH. *Magn Reson Med* 2010;63(6):1456-1462.
15. Yanhua W, Yihang Z, Ying L. Undersampled dynamic magnetic resonance imaging using patch-based spatiotemporal dictionaries. *Biomedical Imaging (ISBI), IEEE 10th International Symposium on*. San Francisco, California, USA,2013. p 294-297.

16. Awate SP, DiBella EVR. Spatiotemporal dictionary learning for undersampled dynamic MRI reconstruction via joint frame-based and dictionary-based sparsity. Biomedical Imaging (ISBI), 9th IEEE International Symposium on. Barcelona, Spain,2012. p 318-321.
17. Lingala SG, Jacob M. Blind compressive sensing dynamic MRI. IEEE Trans Med Imaging 2013;32(6):1132-1145.
18. Ding X, Paisley J, Huang Y, Chen X, Huang F, Zhang X-P. Compressed sensing MRI with Bayesian dictionary learning. Image Processing (ICIP), 20th IEEE International Conference on. Melbourne, Australia,2013. p 2319-2323.
19. Liu Q, Wang S, Yang K, Luo J, Zhu Y, Liang D. Highly undersampled magnetic resonance image reconstruction using two-level bregman method with dictionary updating. IEEE Trans Med Imaging 2013;32(7):1290-1301.
20. Zhang T, Cheng JY, Potnick AG, Barth RA, Alley MT, Uecker M, Lustig M, Pauly JM, Vasanawala SS. Fast pediatric 3D free-breathing abdominal dynamic contrast enhanced MRI with high spatiotemporal resolution. J Magn Reson Imaging 2013;10.1002/jmri.24551.

21. Akçakaya M, Basha TA, Goddu B, Goepfert LA, Kissinger KV, Tarokh V, Manning WJ, Nezafat R. Low-dimensional-structure self-learning and thresholding: regularization beyond compressed sensing for MRI reconstruction. *Magn Reson Med* 2011;66(3):756-767.
22. Wang Y, Ying L. Compressed sensing dynamic cardiac cine MRI using learned spatiotemporal dictionary. *IEEE Trans Biomed Eng* 2014;61(4):1109-1120.
23. Caballero J, Price AN, Rueckert D, Hajnal JV. Dictionary Learning and Time Sparsity for Dynamic MR Data Reconstruction. *IEEE Trans Med Imaging* 2014;33(4):979-994.
24. Elad M, Aharon M. Image denoising via sparse and redundant representations over learned dictionaries. *Ieee Transactions on Image Processing* 2006;15(12):3736-3745.
25. Ravishankar S, Bresler Y. MR image reconstruction from highly undersampled k-space data by dictionary learning. *IEEE Trans Med Imaging* 2011;30(5):1028-1041.
26. Protter M, Elad M. Image Sequence Denoising via Sparse and Redundant Representations. *Ieee Transactions on Image Processing* 2009;18(1):27-35.

27. Winkelmann S, Schaefter T, Koehler T, Eggers H, Doessel O. An optimal radial profile order based on the Golden Ratio for time-resolved MRI. *IEEE Trans Med Imaging* 2007;26(1):68-76.
28. Kim YC, Narayanan SS, Nayak KS. Flexible retrospective selection of temporal resolution in real-time speech MRI using a golden-ratio spiral view order. *Magn Reson Med* 2011;65(5):1365-1371.
29. Lustig M, Pauly JM. SPIRiT: Iterative self-consistent parallel imaging reconstruction from arbitrary k-space. *Magn Reson Med* 2010;64(2):457-471.
30. Fessler JA. On NUFFT-based gridding for non-Cartesian MRI. *J Magn Reson* 2007;188(2):191-195.
31. Morozov V. Solution of Functional Equations by Regularization Method. *Doklady Akademii Nauk Sssr* 1966;167(3):510-&.

## CHAPTER 8

### 8 Future Directions & Conclusion

#### 8.1 Future Directions

There are many areas for improvement of the techniques proposed in this thesis.

Generally, these include improved pulse sequences, fitting models and algorithm implementations.

##### *8.1.1 Cardiac T1 Mapping*

In this thesis, methods for T1 mapping with improved accuracy were discussed as well as sources of error in current clinical T1 mapping sequences. There are two main areas in which T1 mapping can further be improved. These areas are model accuracy /improved pulse sequence design and accelerated mapping. Both of these would lead toward the final goal of accurate and reproducible 3D whole heart T1 mapping.

Currently 2D T1 mapping is the clinical norm and has to be done in multiple slices with slice gaps. Further advances to accelerated cardiac imaging and improved MRI hardware may allow for 3D T1 maps to be acquired in a clinically feasible amount of time (one breath hold).

While 3D T1 maps are desirable, it is important that they also be accurate and consistent. In this thesis, sources of error in the current cardiac T1 mapping technique were noted and some solutions were posed. Improvements to provide for accurate T1 mapping could be an improved fitting method for the current sequence that takes into account all physical parameters. One such way could be Bloch fitting that accounts for

the SSFP readout, off resonance, magnetization transfer and B1 effects. Another method as suggested in the text is to develop a sequence that can easily be fit for T1 without readout error, such as IR-FSE. Currently however, IR-FSE is limited to measuring longer T1 times (due to its readout) and is only applicable for patients with lower heart rates and longer cardiac quiescent periods. Improvements to make this sequence more robust would make it a favorable technique for cardiac T1 mapping.

#### *8.1.2 High SNR High Frame Rate Liver Imaging*

The implementation of PROUD in this thesis is just the tip of the iceberg for applying patch-based image reconstruction constraints for high frame rate MRI. Algorithmic improvements such as reducing computation time would greatly improve the clinical utility of the PROUD method. This could be done through various routes including compilation of the code, multi-threading and GPU implementations. In addition, the temporal performance of the algorithm may be improved by replacing the  $l_2$  norm on the PROUD temporal constraint with an  $L_1$  norm. Further improvements can also be made to the images chosen to make the dictionary in the algorithm. There are endless ways to form the dictionary and a robust exploration of these should be carried out.

In addition, this preliminary work provided results for normal controls. An additional study is warranted for patients with liver disease to understand the ability of PROUD to characterize specific pathologies and also to confirm that the patch-based imaging does not remove any important image textures or small details.

A final future direction could be to utilize perfusion curves derived from temporal PROUD images to carry out a physiological modeling of liver perfusion and provide relevant parameters of liver parenchyma enhancement and tumor enhancement directly for a quantitative and meaningful diagnosis of liver disease.

## 8.2 Conclusion

This thesis has provided solutions for two clinically important needs. Methods for in vivo T1 mapping were explored and sources of error were further understood. In addition, methods to reduce scan time for cardiac applications were introduced. Finally, a new method for high frame rate liver imaging with high SNR was introduced for improved liver imaging and tumor characterization. These methods show the potential for clinical MRI to further improve with reduced scan time (or higher frame rate) and by offering quantitative physiological data in addition to qualitative images.